Large strain and 3D stress analysis of laminated fiber-reinforced soft material structures with high order beam finite elements

Computers and Structures 313 (2025) 107735

Contents lists available at ScienceDirect

Computers and Structures

journal homepage: www.elsevier.com/locate/cas

Large strain and 3D stress analysis of laminated fiber-reinforced soft material structures with high order beam finite elements

Piero Chiaia[1], Alfonso Pagani[2,*], Erasmo Carrera[3]

MUL[2] Lab, Department of Mechanical and Aerospace Engineering, Politecnico di Torino, 10129 Turin, Italy

HIGHLIGHTS

- Equivalent-Single-Layer and Layer-Wise models for hyperelastic laminated structures.
- High-order finite element models to deal with cross-section deformations at high loads.
- Complete three-dimensional stress analysis in highly deformed states.
- Discussion of compatibility and equilibrium conditions in terms of Cauchy's actual stress and reference Piola-Kirchhoff 1 stress.
- Effect of fiber orientation and stacking sequence on the mechanical response is investigated

ARTICLE INFO

Keywords:
Finite element method
Carrera unified formulation
Nonlinear static analysis
Hyperelasticity
Multilayered structures
Stress analysis

ABSTRACT

This study explores the capabilities of higher-order beam models within the Carrera Unified Formulation (CUF) framework for the large strain analysis of multilayered hyperelastic structures made of fiber-reinforced material. These materials exhibit complex mechanical behavior described by both geometrical and material nonlinearities. The proposed approach leverages the strengths of CUF, which allows for the definition of higher-order beam finite elements (FE) whose formal expression is an invariant of the structural theory adopted. The governing equations of the nonlinear static analysis are carried out by the Principle of Virtual Displacements (PVD) in a resulting pure displacement-based formulation. The nonlinear governing equations are written in matrix form in terms of Fundamental Nuclei (FN) of the internal and external force vectors and tangent stiffness matrix. The problem is solved through a Newton–Raphson linearization procedure coupled with path-following methods. The results show the capabilities of higher-order models in terms of accuracy and computational costs in predicting accurate displacements, strains, and detailed 3D stress distributions at large strain. The proposed results are compared with the FE solution obtained through classical models available in commercial software.

1. Introduction

Multilayer materials and structures are of interest for many applications, including but not limited to biological tissues, aerospace composites, and functional and smart devices. Furthermore, new outcomes in mechanical and aerospace engineering, biomechanical applications, renewed interests in composites, laminated structures, and ultra-lightweight components raised by the constant improvements in the manufacturing processes have also posed new challenges in accurately representing the mechanical response of heterogeneous materials.

Finite Element Analysis (FEA) represents one of the most widely used methods in this domain that enabled researchers and engineers to simulate complex behaviors of materials and structures under varying conditions. The accurate analysis of components and structures nowadays demands high-fidelity numerical simulations, eventually coupled with efficient calculation paradigms and digital twinning techniques to accommodate real-time characterization of the mechanical response for certain applications, e.g., structural health monitoring in aerospace or personalized medical treatments and surgery.

* Corresponding author.
Email addresses: piero.chiaia@polito.it (P. Chiaia), alfonso.pagani@polito.it (A. Pagani), erasmo.carrera@polito.it (E. Carrera).
[1] PhD student.
[2] Full Professor.
[3] Professor of Aerospace Structures and Aeroelasticity.

https://doi.org/10.1016/j.compstruc.2025.107735
Received 5 October 2024; Accepted 5 March 2025
Available online 18 March 2025

Aerospace engineering relies heavily on composites for components requiring lightweight, high-strength materials and highly flexible structures [1]. Fiber-reinforced polymers (FRPs), such as carbon fiber-reinforced epoxy composites, sandwich structures with metallic foam cores, and soft elastomers with stiffer fibers [2] are extensively adopted thanks to their enhanced strength properties. In mechanical engineering, elastomers like silicone rubber [3] and short glass fiber-reinforced polyamide [4], commonly used in seals, gaskets, and shock absorbers, exhibit highly nonlinear mechanical responses also at low to moderate load regimes due to their low stiffness [5]. These materials, however, show hysteresis and dissipation when cyclic loads are considered, necessitating accurate modeling techniques for predicting their performance in various applications [6]. Also, elastomers present multi-field physical behavior and are practically used in dielectric sensor devices [7]. These materials' high extensibility and elastic properties are also investigated in fluid-structure interaction problems [8,9].

Biological tissue, essential for physiological functions, is typically modeled in the field of anisotropic hyperelasticity such as elastin layers of arterial walls and collagen fibers [10]; musculoskeletal tissues like tendons and ligaments allow efficient energy storage and transmission during movement. The mechanical properties possessed by the hyperelastic material behavior are additionally extended by peculiar softening and hardening behavior [11], given by the presence of continuous fiber reinforcement that characterizes the strong anisotropic behavior of these tissues [12].

In the field of computational mechanics and finite element (FE) models, modeling hyperelastic materials is a challenging task due to their ability to undergo huge elastic deformations characterized by a nonlinear stress–strain relationships (material nonlinearities) [13,14]. Accurate and efficient numerical models that take into account large strains (geometrical nonlinearities) of these materials require, in general, higher-order formulations and alleviate numerical limitations that arise in such nonlinear problems, such as volumetric locking in nearly-incompressible hyperelastic materials [15,16]. Refined or computationally expensive models are required when cross-section warping and twisting effects are taken into account in the displacement, strain and stress field. Within this context, many FE procedures to deal with these complex deformation states have been proposed over the years, see [17–20], as well as novel numerical models for complex stress state prediction due to interfacial effects and non-uniform material properties across the layers [21,22]. Moreover, stress components within the material are strongly influenced by the type of load applied (conservative and nonconservative), so it becomes necessary to analyze in detail the stress tensors typically adopted in the formulation of a finite element model (the second Piola–Kirchhoff and Cauchy stress tensor) see [23–25].

Recently, refined fully nonlinear FE models have been developed in the well-established Carrera Unified Formulation (CUF) framework to simulate multilayered structures in various fields. The capabilities of higher-order beam, plate, and shell models have been tested in various engineering applications, see [26–28]. In general, CUF enables the definition of FE formulation, based on the theory of structure approximation of any order, in terms of Fundamental Nuclei (FN), the basic building blocks of the present approach. In the field of hyperelasticity, this formulation has been recently extended to analyze also hyperelastic beams, plates, and shell structures, see [29–31].

In this work, higher-order beam (1D) models are employed to study laminated fiber-reinforced hyperelastic soft structures, exploiting the modeling approach allowed by CUF, with particular emphasis on the analysis of complex 3 D stress states arising in large strain problems. The present work is organized as follows: (i) first, the continuum mechanics formalism adopted to introduce the general hyperelastic framework and finite element models is presented in Section 2; (ii) second, the hyperelastic constitutive law for isotropic and anisotropic soft materials is introduced, introducing the general strain and stress measures adopted in Section 3; (iii) third, the Unified Formulation of beam theories, adopted in the present work, is presented in Section 4, introducing the CUF formalism and the coupling of kinematic models and cross-section expansion theories; (iv) fourth, the governing equations for the nonlinear static analysis are derived in terms of variational principle, and the matrix form of the nonlinear static problem is introduced in terms of FN of finite element matrices. Also, the numerical scheme proposed to obtain the solution of the nonlinear problem is presented in Section 5; (v) subsequently, the benchmark problems proposed are discussed in Section 6, presenting the numerical results obtained adopting higher-order 1D CUF models and comparing actual proposed results with reference solutions obtained via the commercial code ABAQUS; (vi) finally, the main conclusions are discussed in Section 7.

2. Total lagrangian formulation and internal strain energy

Consider a deformable continuum body subjected to constraints and external forces. From the definition of the deformation function, one can define the classical displacement and strain measures adopted in continuum mechanics. The deformation gradient is defined starting from the Lagrangian displacement field $\mathbf{U}(\mathbf{X},t) = \boldsymbol{x}(\mathbf{X},t) - \mathbf{X}$:

$$\mathbf{F}(\mathbf{X},t) = \frac{\partial \mathbf{f}(\mathbf{X},t)}{\partial \mathbf{X}} = \mathrm{Grad}\boldsymbol{x}(\mathbf{X},t) \tag{1}$$

In the following, the determinant of the deformation gradient is defined as J, which is related to the local volume change. Subsequently, one can define the right Cauchy–Green strain tensor $\mathbf{C}$ and the Green–Lagrange strain tensor $\mathbf{E}$:

$$\mathbf{C}(\mathbf{X},t) = \mathbf{F}^T\mathbf{F} \tag{2}$$

$$\mathbf{E}(\mathbf{X},t) = \frac{1}{2}(\mathbf{F}^T\mathbf{F} - \mathbf{I}) \tag{3}$$

Typically, hyperelastic mathematical models are defined starting from the invariants of the right Cauchy–Green strain tensor, following objectivity arguments and independence from the reference frame [32]; thus, one can define:

$$I_1 = \mathrm{tr}(\mathbf{C}) \tag{4}$$

$$I_2 = \frac{1}{2}((\mathrm{tr}(\mathbf{C}))^2 - \mathrm{tr}(\mathbf{C}^2)) \tag{5}$$

$$I_3 = \det(\mathbf{C}) = \det(\mathbf{F}^T\mathbf{F}) = J^2 \tag{6}$$

where $\mathrm{tr}(\cdot)$ and $\det(\cdot)$ are the trace and the determinant operators, respectively.

Consider the continuum body at equilibrium. The internal stress can be described by the Cauchy's traction vector $\mathbf{t}(\boldsymbol{x},t,\mathbf{n}) = \boldsymbol{\sigma}(\boldsymbol{x},t)\mathbf{n}$ in the actual configuration, related to the Cauchy's stress tensor $\boldsymbol{\sigma}$, or the first Piola–Kirchhoff traction vector $\mathbf{T}(\mathbf{X},t,\mathbf{N}) = \boldsymbol{P}(\mathbf{X},t)\mathbf{N}$, related to the first Piola–Kirchhoff stress tensor (PK1) $\boldsymbol{P}$, for the reference configuration [33]. Furthermore, the second Piola–Kirchhoff stress tensor (PK2) is related to the tensor $\boldsymbol{\sigma}$ by a Piola transform:

$$\boldsymbol{\sigma} = \frac{1}{J}\mathbf{F}\mathbf{S}\mathbf{F}^{-1} \tag{7}$$

In the Total Lagrangian approach adopted in the present finite element scenario, the equation of motion is considered in the reference configuration state:

$$\mathrm{Div}\mathbf{P} + \mathbf{B} = 0 \tag{8}$$

3. Anisotropic hyperelasticity

3.1. Strain energy function and constitutive law

Fiber-reinforced soft materials are typically modeled in the framework of large elastic deformations. In the hyperelastic material framework, the strain energy function Ψ is defined starting from the invariants and pseudo-invariants of the deformation, depending on the mechanical properties of the soft material considered. The dependence on the continuous fiber reinforcement in soft fibrous tissues is exploited embedding the preferential direction is in the definition of Ψ by means of a structural tensor. In the Cartesian reference frame, if the fiber direction is described by the unit vector $\mathbf{a}_0 = (a_x, a_y, a_z)^T$, the strain energy function for a general transversely isotropic hyperelastic material is expressed as:

$$\Psi = \Psi(\mathbf{C}, \mathbf{a}_0 \otimes \mathbf{a}_0) \tag{9}$$

where $(\cdot)\otimes(\cdot)$ stands for the dyadic product operator. From this starting point, Ψ is then expressed as a function of the three classical principal invariants of $\mathbf{C}$ and two additional pseudo-invariants, by which the dependence of the fiber-reinforcement direction is incorporated and objectivity is still verified [33]:

$$I_4 = \mathbf{a}_0 \cdot \mathbf{C}\mathbf{a}_0 \tag{10}$$

$$I_5 = \mathbf{a}_0 \cdot \mathbf{C}^2\mathbf{a}_0 \tag{11}$$

Therefore, the general hyperelastic strain energy function is written as:

$$\Psi = \Psi(I_1(\mathbf{C}), I_2(\mathbf{C}), I_3(\mathbf{C}), I_4(\mathbf{C}, \mathbf{a}_0), I_5(\mathbf{C}, \mathbf{a}_0)) \tag{12}$$

In nearly-incompressible hyperelastic materials, the volume ratio coefficient J is approaching the unity, thus also I_3. Anisotropic soft tissues are analyzed considering then direction-dependent free energy, from which the general constitutive law is derived. In this work, both isotropic and transversly isotropic materials are considered.
In the literature, commonly adopted models are defined starting from the decoupled formulation of strain energy functions [34], namely Ψ is written as the sum of purely independent components representing each different material behavior:

$$\Psi = \Psi_{vol}(J) + \bar{\Psi}_{iso}(\bar{I}_1, \bar{I}_2) + \bar{\Psi}_{aniso}(\bar{I}_1, \bar{I}_2, \bar{I}_4, \bar{I}_5) \tag{13}$$

where $\bar{\Psi}_{iso}$ and $\bar{\Psi}_{aniso}$ depend on the rescaled isotropic invariants, namely invariants $(\bar{I}_1, \bar{I}_2, \bar{I}_3)$ of $\bar{\mathbf{C}} = J^{-2/3}\mathbf{C}$ and anisotropic rescaled invariants $\bar{I}_4 = J^{-2/3}I_4$ and $\bar{I}_5 = J^{-4/3}I_5$. For a more detailed description of the model see [33].

In the proposed paper, the hyperelastic framework is modeled in the coupled formulation, deriving the closed-form expression of the constitutive law starting from the more general definition of Ψ, Eq. (12). Considering the material model given by the expression of the strain energy function, the constitutive law in the material reference frame, namely the stress–strain relation, is given by:

$$\mathbf{S} = 2\frac{\partial\Psi(\mathbf{C})}{\partial\mathbf{C}} + \left[\left(\frac{\partial\Psi}{\partial I_1} + I_1\frac{\partial\Psi}{\partial I_2}\right)\mathbf{I} - \frac{\partial\Psi}{\partial I_2}\mathbf{C} + I_3\frac{\partial\Psi}{\partial I_3}\mathbf{C}^{-1} + \frac{\partial\Psi}{\partial I_4}\mathbf{a}_0\otimes\mathbf{a}_0 + \frac{\partial\Psi}{\partial I_5}\left(\mathbf{a}_0\otimes\mathbf{C}\mathbf{a}_0 + \mathbf{a}_0\mathbf{C}\otimes\mathbf{a}_0\right)\right] \tag{14}$$

3.2. Incremental formulation and tangent elasticity tensor

In a general numerical framework for nonlinear elasticity, an incremental formulation is adopted to solve the nonlinear governing equations that take into account both geometric and material nonlinearities. The constitutive law Eq. (14) can be rewritten in an incremental form:

$$\Delta\mathbf{S} = \mathbb{C} : \frac{1}{2}\Delta\mathbf{C} = \mathbb{C} : \Delta\mathbf{E} \tag{15}$$

where $\mathbb{C}$ is the tangent elasticity tensor, under the coupled formulation of hyperelasticity, is here given by:

$$\mathbb{C} = 2\frac{\partial\mathbf{S}(\mathbf{C})}{\partial\mathbf{C}} = \frac{\partial\mathbf{S}(\mathbf{E})}{\partial\mathbf{E}} = 4\frac{\partial^2\Psi}{\partial\mathbf{C}\partial\mathbf{C}} \tag{16}$$

The analytical expression of the tangent elasticity tensor can be found in [33].

4. Higher-order beam models

The present work adopts a displacement-based finite element model based on CUF to analyze multilayered isotropic and fiber-reinforced hyperelastic beams. These finite element models are well-established in the literature, and an extensive description of the adopted approach can be found in [35]. In the unified formulation of beam theories, the 3 D displacement field is provided as a formal expression independent of the structural theory considered, which is an analysis input describing the cross-section kinematics:

$$\mathbf{u}(x, y, z) = F_\tau(x, z)\mathbf{u}_\tau(y) \qquad \tau = 1, \dots, M \tag{17}$$

where F_τ is the set of cross-section expansion polynomials adopted depending on the structural theory, M is the dimension of the set of expansion basis functions, and $\mathbf{u}_\tau$ is the vector of generalized displacement components along the beam axis direction. The choice of F_τ to model the cross-section kinematics and the polynomial order of expansion is arbitrary; in this way, any structural theory can be included in the model of the displacement field without any loss of generality. A graphical representation of 1D CUF models is proposed in Fig. 1.
In the following, the Einstein notation is adopted; thus, repeated subscript τ indicates summation. Generally, two sets of expansion functions are adopted in the unified formulation of beam theories, depending on the nature of the cross-section kinematics. In the present work, both Taylor (TE models) and Lagrange polynomials (LE models) are exploited [35].

Adopting Taylor polynomials as F_τ expansion function led to the Equivalent-Single-Layer model (ESL). In these models, the displacement field of the beam is seen as a homogenized field obtained starting from each cross-section sub-component [35]. The generalized displacement field, up to a certain polynomial degree, is obtained by summing the generalized unknowns, which are the higher-order derivatives of the displacement components. Considering the chosen expansion order M, which is again an input parameter of the FE model proposed, higher-order theories are defined hierarchically. In TE models, 2 D MacLaurin polynomials are adopted as cross-section expansion of the generalized displacements. Higher-order theories are defined automatically thanks to the hierarchical nature of MacLaurin polynomials, where the series of polynomials adopted of the type $x^i z^j$ is expanded up to the M-th order. As an example, the TE-2 higher-order theory with constant, linear, and parabolic expansion terms is:

$$\begin{cases} u_x(x,y,z) = u_{x_1}(y) + xu_{x_2}(y) + zu_{x_3}(y) + x^2u_{x_4}(y) + xzu_{x_5}(y) + z^2u_{x_6}(y) \\ u_y(x,y,z) = u_{y_1}(y) + xu_{y_2}(y) + zu_{y_3}(y) + x^2u_{y_4}(y) + xzu_{y_5}(y) + z^2u_{y_6}(y) \\ u_x(x,y,z) = u_{z_1}(y) + xu_{z_2}(y) + zu_{z_3}(y) + x^2u_{z_4}(y) + xzu_{z_5}(y) + z^2u_{z_6}(y) \end{cases} \tag{18}$$

where, u_{x_i}, u_{y_i} and u_{z_i}, $i = 1\dots 10$, are the generalized beam displacements. In the present approach, classical beam theories, such as Euler–Bernoulli Beam Theory (EBBT) and Timoshenko Beam Theory (TBT), are considered particular cases of the $M = 1$ TE model [35].

Instead, LE models are based on discretizing the cross-section into several local beam sub-domains, over which Lagrange's polynomials are defined to interpolate the cross-section displacement field. This approach leads to the definition of local independent discretizations for

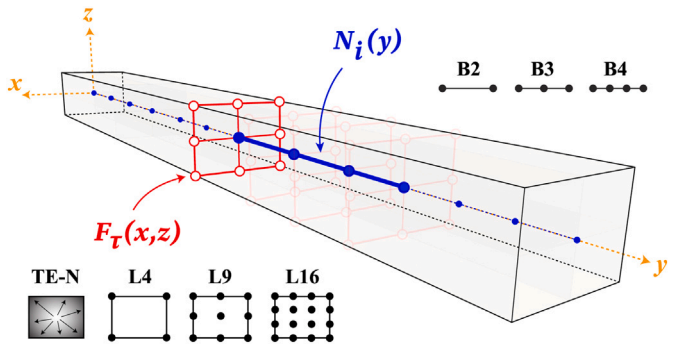

Fig. 1. Higher-order 1D CUF models.

each beam sub-component. In this way, different kinematic models can be assigned independently from those of other components. Thus, refined local cross-section models can be arbitrarily obtained. For this reason, LE models are also addressed as a Layer-Wise (LW) models, obtaining a pure displacement-based model in which the generalized unknowns correspond exactly with the 3 D component of the displacement field. As an example, the displacement field of an L4 linear expansion model is reported, expressed as:

$$\begin{cases} u_x(x,y,z) = F_1(x,z)u_{x_1}(y) + F_2(x,z)u_{x_2}(y) + F_3(x,z)u_{x_3} + F_4(x,z)u_{x_4}(y) \\ u_y(x,y,z) = F_1(x,z)u_{y_1}(y) + F_2(x,z)u_{y_2}(y) + F_3(x,z)u_{y_3} + F_4(x,z)u_{y_4}(y) \\ u_z(x,y,z) = F_1(x,z)u_{z_1}(y) + F_2(x,z)u_{z_2}(y) + F_3(x,z)u_{z_3} + F_4(x,z)u_{z_4}(y) \end{cases} \tag{19}$$

In this sense, 1D-CUF LE expansion models are referred to as four-node linear L4, nine-node parabolic L9, and quadratic six-node cubic L16 cross-section expansion models. Exploiting the isoparametric formulation, Lagrange's polynomials are defined in the natural reference frame. Therefore, all physical quantities required are computed by the natural coordinates and change of variables expressed by the Jacobian. Once the refined structural theory adopted is fixed, the generalized unknowns along the beam axis $\mathbf{u}_\tau(y)$ of the beam axis domain are discretized by adopting the classical FE approach:

$$\mathbf{u}_\tau(y) = N_i(y)\mathbf{u}_{\tau i} \qquad i = 1, \dots, N_n \tag{20}$$

where the continuous displacement field along the beam axis is further discretized considering a linear combination of finite displacement components $\mathbf{u}_{\tau i}$ expanded by the $N_i(y)$ 1D shape functions, the former are final unknowns of the model, and N_n is the total number of finite nodes per element adopted. The final expression of the 3-D displacement field in the CUF domain can be seen as a coupled expansion of structural beam theories and kinematic models along the beam axis, modeled in a single unified expression:

$$\mathbf{u}(x,y,z) = F_\tau(x,z)\mathbf{u}_\tau(y) = F_\tau(x,z)N_i(y)\mathbf{u}_{\tau i} \tag{21}$$

The classical 1D shape functions are addressed as linear B2, parabolic B3, and cubic B4 finite interpolation along the beam axis, explicitly indicating the total number of finite nodes adopted. The 1D Lagrange shape functions are again defined starting from the total number of nodes involved. Starting from Eq. (21), any displacement-based model can be obtained hierarchically by choosing the two independent polynomial bases for the axis and cross-section kinematics. In both ESL and LW models, displacement continuity is naturally achieved from the FE matrices assembling procedures' point of view. The assembling procedures for ESL and LW models are presented in Fig. 2. Furthermore, the regularity conditions for displacements and transverse stress distributions, the C_z^0 requirements [36], have been assessed for higher-order structural theories, predicting efficiently accurate 3 D stress distributions and avoiding inconsistent solutions when transverse out-of-plane normal and transverse shear stresses at the beam edges are considered [37]. In addition, the adoption of higher-order beam models implemented straightforwardly in this scenario deal efficiently with coupled three-dimensional local effects, such as warping or twisting, captured by the enriched kinematics of the displacement field, up to any order, avoiding ad-hoc correction techniques. The capabilities and the accuracy of the present higher-order 1D beam models have been established in literature analyzing complex three-dimensional strain and stress states of thin walled structures [38], the effects of large displacements and rotations [39,40] both in the field of geometrical and material nonlinearities, as done in [31].

5. Nonlinear governing equations in matrix form

5.1. Real and virtual measures

The nonlinear governing equation in weak form is carried out by the PVD:

$$\delta\mathcal{L}_{int} = \delta\mathcal{L}_{ext} \tag{22}$$

where $\mathcal{L}_{int}$ is the internal strain energy, $\mathcal{L}_{ext}$ is the work done by external loads, and δ denotes the virtual variation. Referring to a Total Lagrangian formulation, these terms are expressed in terms of physical quantities defined in the material reference frame; thus the PK2 stress tensor $\mathbf{S}$ and the full Green–Lagrange strain tensor $\mathbf{E}$ are adopted. Introducing now Voigt's notation for symmetric tensors, physical quantities are rewritten in vector form as follows:

$$\boldsymbol{S} = \{S_{xx}, S_{yy}, S_{zz}, S_{xz}, S_{yz}, S_{xy}\}^T \tag{23}$$

$$\boldsymbol{E} = \{E_{xx}, E_{yy}, E_{zz}, E_{xz}, E_{yz}, E_{xy}\}^T \tag{24}$$

The full Green–Lagrange strain tensor is rewritten in terms of generalized nodal displacements and expansion functions with the same index notation adopted for the displacement field [29,31]:

$$\boldsymbol{E} = (\mathbf{b}_l + \mathbf{b}_{nl})\,\mathbf{u} = (\mathbf{b}_l + \mathbf{b}_{nl})\,F_\tau(x,z)N_i(y)\mathbf{u}_{\tau i} = (\mathbf{B}_l^{\tau i} + \mathbf{B}_{nl}^{\tau i})\mathbf{u}_{\tau i} \tag{25}$$

Applying the formal matrices of derivatives operator $\mathbf{b}_l$ and $\mathbf{b}_{nl}$, whose formal expression can be found in [41], to the polynomial expansion of the displacement field, the algebraic matrices $\mathbf{B}_l^{\tau i}$ and $\mathbf{B}_{nl}^{\tau i}$ are therefore defined:

$$\mathbf{B}_l^{\tau i} = \begin{bmatrix} F_{\tau,x}N_i & 0 & 0 \\ 0 & F_\tau N_{i,y} & 0 \\ 0 & 0 & F_{\tau,z}N_i \\ F_{\tau,z}N_i & 0 & F_{\tau,x}N_i \\ 0 & F_{\tau,z}N_i & F_\tau N_{i,y} \\ F_\tau N_{i,y} & F_{\tau,x}N_i & 0 \end{bmatrix} \tag{26}$$

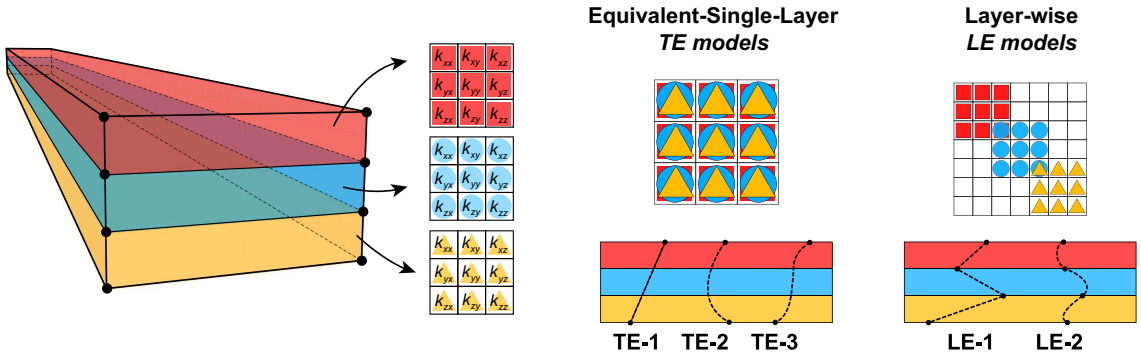

Fig. 2. Unified models: equivalent-single-layer and layer-wise models.

$$\mathbf{B}_{nl}^{\tau i} = \frac{1}{2}\begin{bmatrix} u_{x,x}F_{\tau,x}N_i & u_{y,x}F_{\tau,x}N_i & u_{z,x}F_{\tau,x}N_i \\ u_{x,y}F_{\tau}N_{i,y} & u_{y,y}F_{\tau}N_{i,y} & u_{z,y}F_{\tau}N_{i,y} \\ u_{x,z}F_{\tau,z}N_i & u_{y,z}F_{\tau,z}N_i & u_{z,z}F_{\tau,z}N_i \\ u_{x,x}F_{\tau,z}N_i + u_{x,z}F_{\tau,x}N_i & u_{y,x}F_{\tau,z}N_i + u_{y,z}F_{\tau,x}N_i & u_{z,x}F_{\tau,z}N_i + u_{z,z}F_{\tau,x}N_i \\ u_{x,y}F_{\tau,z}N_i + u_{x,z}F_{\tau}N_{i,y} & u_{y,y}F_{\tau,z}N_i + u_{y,z}F_{\tau}N_{i,y} & u_{z,y}F_{\tau,z}N_i + u_{z,z}F_{\tau}N_{i,y} \\ u_{x,x}F_{\tau}N_{i,y} + u_{x,y}F_{\tau,x}N_i & u_{y,x}F_{\tau}N_{i,y} + u_{y,y}F_{\tau,x}N_i & u_{z,x}F_{\tau}N_{i,y} + u_{z,y}F_{\tau,x}N_i \end{bmatrix} \tag{27}$$

where the symbol $(\cdot)_{,(\cdot)}$ stands for the partial derivation operator.

In a finite element scenario, the virtual variation of physical quantities is required. Adopting the same index notation and polynomial expansion previously introduced for the real displacement field, the virtual variation of displacements and strains is exploited by independent indices, namely here the j index for beam axis nodes and the s index for the 1D CUF expansion theory, to obtain independent quantities with respect to real ones. In this way, the virtual displacement field is:

$$\delta\mathbf{u}(x,y,z) = F_s(x,z)\delta\mathbf{u}_s(y) = F_s(x,z)N_j(y)\delta\mathbf{u}_{sj} \;\; j = 1,2,..,N_n, \;\; s = 1,\dots,M \tag{28}$$

The virtual variation of the strain measure is written again in compact form following the previous procedure explicated in Eq. (25):

$$\delta\boldsymbol{E} = \delta((\mathbf{B}_l^{\tau i} + \mathbf{B}_{nl}^{\tau i})\mathbf{u}_{\tau i}) = (\mathbf{B}_l^{sj} + 2\mathbf{B}_{nl}^{sj})\delta\mathbf{u}_{sj} \tag{29}$$

5.2. Nonlinear static problem

Starting from the previously introduced physical quantities, the matrix-form of the static equilibrium problem is carried out following Eq. (22). From the definition:

$$\delta\mathcal{L}_{int} = \int_\Omega \delta\boldsymbol{E}^T\boldsymbol{S}dV = \int_\Omega \delta\mathbf{u}_{sj}^T(\mathbf{B}_l^{sj} + 2\mathbf{B}_{nl}^{sj})^T\boldsymbol{S}dV = \delta\mathbf{u}_{sj}^T\mathbf{F}_{int}^{sj} \tag{30}$$

where $\mathbf{F}_{int}^{sj}$ the 3x1 FN of the internal forces vector:

$$\mathbf{F}_{int}^{sj} = \int_\Omega (\mathbf{B}_l^{sj} + 2\mathbf{B}_{nl}^{sj})^T\boldsymbol{S}dV \tag{31}$$

Referring to the external load contribution in the variational principle, the FN of the external load vector is exploited by means of the same derivation procedure described for the internal energy contribution. If $\mathbf{f}$ is the vector of external loads applied to the structure, one has

$$\delta\mathcal{L}_{ext} = \int_\Omega \delta\boldsymbol{u}^T\mathbf{f}dV = \int_\Omega \delta\mathbf{u}_{sj}^T F_s(x,z)N_j(y)\mathbf{f}\;dV = \delta\mathbf{u}_{sj}^T\mathbf{F}_{ext}^{sj} \tag{32}$$

where $\mathbf{F}_{ext}^{sj}$ the 3x1 FN of the external forces vector:

$$\mathbf{F}_{ext}^{sj} = \int_\Omega F_s(x,z)N_j(y)\mathbf{f}\;dV \tag{33}$$

The final governing equation in matrix form is then written as:

$$\delta\mathbf{u}_{sj}^T\mathbf{F}_{int}^{sj} = \delta\mathbf{u}_{sj}^T\mathbf{F}_{ext}^{sj} \quad \rightarrow \quad \delta\mathbf{u}_{sj} : \;\; \mathbf{F}_{int}^{sj} = \mathbf{F}_{ext}^{sj} \tag{34}$$

Considering the summation over indices s and j, the global internal forces vector $\mathbf{F}_{int}$ and external load vector $\mathbf{F}_{int}$ can be computed, following the CUF assembling procedure [35]. In a CUF-based finite element model, the final governing equations are written in terms of FNs, as shown in Eq. (34), which are defined regardless of the specific theory of structure approximation adopted, represented by F_τ and F_s cross-section expansion functions, or kinematic models along the beam axis, represented by N_i and N_j shape functions. In this sense, the key feature of a CUF-based finite element model explored for the hyperelastic framework is to derive the governing equations regardless of the mathematical models adopted in the FE implementation. In particular, in this proposed model, thanks to CUF, the C_z^0 requirement for the displacement component is obtained straightforwardly following the classical assembling procedure of finite element matrices as detailed in Section 4. The specific FN of internal and external forces are obtained by assigning the polynomial basis set and exploiting the summation over indices.

5.3. Linearized governing equation and numerical solver

In a finite element scenario for hyperelasticity, both large displacements, rotations and strains (geometrical nonlinearities) and nonlinear constitutive law (material nonlinearities) are taken into account.

Therefore, the equilibrium equations Eq. (34) turn out to be strongly nonlinear. Common solution techniques are based on iterative solvers using linearized incremental procedures. The nonlinear problem Eq. (34) is written as an equivalent optimization problem in the form of minimization of the residual function [42]. Defining the unbalanced nodal forces vector as:

$$\varphi_{res}(\mathbf{u},\mathbf{f}) \equiv \mathbf{F}_{int} - \mathbf{F}_{ext} \tag{35}$$

one can find the non-trivial equilibrium state as the root of Eq. (35) since, at equilibrium, due to balance, the residual nodal forces vector is null ($\varphi_{res} = 0$). In the present approach, the Newton–Raphson incremental-iterative solver is employed. The residual nodal forces vector is written considering a Taylor's expansion around a known condition $(\mathbf{u}^k, \mathbf{f}^k)$, truncated at the first order, of an increment $(\Delta\mathbf{u}^k, \Delta\mathbf{f}^k)$:

$$\varphi_{res}(\mathbf{u}^k + \Delta\mathbf{u}^k, \mathbf{f}^k + \Delta\mathbf{f}^k) = \varphi_{res}(\mathbf{u}^k, \mathbf{f}^k) + \left.\frac{\partial \varphi_{res}}{\partial \mathbf{u}}\right|_{(\mathbf{u}^k,\mathbf{f}^k)} \Delta\mathbf{u}^k + \left.\frac{\partial \varphi_{res}}{\partial \mathbf{f}}\right|_{(\mathbf{u}^k,\mathbf{f}^k)} \Delta\mathbf{f}^k \tag{36}$$

Under the hypothesis of conservative loads, $\mathbf{f}$ does not depend on the deformed configuration ($\mathbf{f}$ is considered here as a dead load and not a follower load), the finite variation of the load vector can be rearranged and written in terms of the load factor λ:

$$\Delta\mathbf{f}^k = \Delta(\lambda \mathbf{f}^k_{ref}) = \Delta\lambda^k \mathbf{f}_{ref} \tag{37}$$

Defining the tangent stiffness matrix as $\frac{\partial \varphi_{res}}{\partial \mathbf{u}} = \mathbf{K}_T$ and recognizing that $\frac{\partial \varphi_{res}}{\partial \mathbf{f}} = -\mathbf{I}$, the equilibrium condition in terms of residual forces vector is then imposed, $\varphi_{res}(\mathbf{u}^k + \Delta\mathbf{u}^k, \mathbf{f}^k + \Delta\mathbf{f}^k) = 0$. Finally, the incremental equation Eq. (36) is rearranged, obtaining:

$$\mathbf{K}_T(\mathbf{u}^k)\Delta\mathbf{u}^k = \Delta\lambda^k \mathbf{f}_{ref} - \varphi_{res}(\mathbf{u}^k, \mathbf{f}^k) \tag{38}$$

In the final form of the incremental equation Eq. (38), two unknowns are present: the finite variations $\Delta\mathbf{u}^k$ and $\Delta\lambda^k$. Since the loading scale parameter λ is an additional variable, Eq. (38) is coupled with an additional constraint equation, to close algebraically the problem, thus:

$$\begin{cases} \mathbf{K}_T(\mathbf{u}^k)\Delta\mathbf{u}^k = \Delta\lambda^k \mathbf{f}_{ref} - \varphi_{res}(\mathbf{u}^k, \mathbf{f}^k) \\ c(\Delta\mathbf{u}^k, \Delta\lambda^k) = 0 \end{cases} \tag{39}$$

The final system of equations is solved to obtain the new updated configuration $(\mathbf{u}^{k+1}, \mathbf{f}^{k+1}) = (\mathbf{u}^k + \Delta\mathbf{u}^k, \mathbf{f}^k + \Delta\mathbf{f}^k)$. The present procedure is repeated iteratively up to a certain convergence tolerance on the unbalanced nodal forces vector, namely $|\varphi_{res}| < \varepsilon$. In the proposed solver, convergence criteria are also imposed on the $\Delta\mathbf{u}^k$ and $\Delta\lambda^k$, to correctly predict snap-back or snap-through phenomena [43]. The constraint equation characterizes the numerical procedure adopted, implementing then the so-called displacement and load control method, or path-following methods such as arc-length type searching method. In the following, the path-following method as proposed by Crisfield [44] and later modified by Carrera [43] is adopted. More details about the implementation of incremental-iterative solver in a CUF-based finite element method for geometrically nonlinear and hyperelastic problems can be explicitly found in [41,45].

The following adopted arc-length-based solver for the nonlinear equilibrium equations is based on the implementation of the classical additional constraint equation for the possible nodal displacement increment, following the path-following approach. In particular, the constraint equation adopted is practically a multi-dimensional constraint, given by a multi-dimensional sphere of possible updated configurations. This sphere is centered at $\mathbf{u}_k$ with a radius equal to L_0, defined as follows:

$$(L_0)^2 = (\Delta u^{(k)}) \cdot (\Delta u^{(k)}) \tag{40}$$

Here, the subscript (k) denotes the generic k-th equilibrium status of the last convergent equilibrium state. Adopting this constraint relation for the admissible generic increment, also the load scale parameter λ is restricted. Equation (40) serves as the starting point for deriving the corresponding constraint equation for the load factor increment. For a more comprehensive examination of path-following methods and arc-length type solvers, the reader can refer to [43].

5.4. Tangent stiffness matrix

Following the definition of internal and external forces FN, in the present section the FN of the tangent stiffness matrix is derived. Under the assumption of conservative external loads, the FN of the tangent matrix is derived from the linearization of the internal forces vector:

$$\Delta(\delta\mathcal{L}_{int}) = \int_\Omega \Delta(\delta \boldsymbol{E}^T \boldsymbol{S}) dV = \int_\Omega \delta \boldsymbol{E}^T \Delta\boldsymbol{S} dV + \int_\Omega \Delta(\delta \boldsymbol{E}^T)\boldsymbol{S} dV \tag{41}$$

The first term in Eq. (41) represents the contribution given by the linearization of the constitutive law. Adopting Holzapfel's formulation, Eq. (15) is rewritten in matrix form exploiting Voigt notation:

$$\Delta\mathbf{S} = \mathbb{C}\frac{1}{2}\Delta\mathbf{C} = \mathbb{C}\Delta\mathbf{E} = \mathbb{C}(\mathbf{B}^{\tau i}_l + 2\mathbf{B}^{\tau i}_{nl})\Delta\mathbf{u}_{\tau i} \tag{42}$$

Thus, the term related to the linearized constitutive law is explicitly written as:

$$\begin{aligned} \int_\Omega \delta \boldsymbol{E}^T \Delta\boldsymbol{S} dV &= \int_\Omega \delta\mathbf{u}^T_{sj}(\mathbf{B}^{sj}_l + 2\mathbf{B}^{sj}_{nl})^T \mathbb{C}(\mathbf{B}^{\tau i}_l + 2\mathbf{B}^{\tau i}_{nl})\Delta\mathbf{u}_{\tau i}\, dV \\ &= \delta\mathbf{u}^T_{sj}\mathbf{K}^{\tau sij}_{ll}\Delta\mathbf{u}_{\tau i} + \delta\mathbf{u}^T_{sj}\mathbf{K}^{\tau sij}_{lnl}\Delta\mathbf{u}_{\tau i} + \delta\mathbf{u}^T_{sj}\mathbf{K}^{\tau sij}_{nll}\Delta\mathbf{u}_{\tau i} \\ &\quad + \delta\mathbf{u}^T_{sj}\mathbf{K}^{\tau sij}_{nlnl}\Delta\mathbf{u}_{\tau i} \\ &= \delta\mathbf{u}^T_{sj}\mathbf{K}^{\tau sij}_{ll}\Delta\mathbf{u}_{\tau i} + \delta\mathbf{u}^T_{sj}\mathbf{K}^{\tau sij}_{T_1}\Delta\mathbf{u}_{\tau i} \end{aligned} \tag{43}$$

where $\mathbf{K}^{\tau sij}_{ll}$ is the FN of linear contribution of the tangent matrix and $\mathbf{K}^{\tau sij}_{T_1} = \mathbf{K}^{\tau sij}_{lnl} + \mathbf{K}^{\tau sij}_{nll} + \mathbf{K}^{\tau sij}_{nlnl}$ is the non linear contribution.

The second term of Eq. (41) is FN of the geometrical stiffness matrix $\mathbf{K}^{\tau sij}_{\sigma}$, stemming from the linearization of the geometrical relations:

$$\int_\Omega \Delta(\delta \boldsymbol{E})^T \boldsymbol{S} dV = \delta\mathbf{u}^T_{sj}\mathbf{K}^{\tau sij}_{\sigma}\Delta\mathbf{u}_{\tau i} \tag{44}$$

The derivation will not be reported here but can be found explicitly in [41,45]. Substituting these FN definitions in Eq. (41), the analytic closed-form expression of FN tangent stiffness matrix in terms of linear, nonlinear and geometrical stiffness matrix FNs is:

$$\begin{aligned} \Delta(\delta\mathcal{L}_{int}) &= \int_\Omega \delta \boldsymbol{E}^T \Delta\boldsymbol{S} dV + \int_\Omega \Delta(\delta \boldsymbol{E})^T \boldsymbol{S} dV \\ &= \delta\mathbf{u}^T_{sj}\mathbf{K}^{\tau sij}_{ll}\Delta\mathbf{u}_{\tau i} + \delta\mathbf{u}^T_{sj}\mathbf{K}^{\tau sij}_{T_1}\Delta\mathbf{u}_{\tau i} + \delta\mathbf{u}^T_{sj}\mathbf{K}^{\tau sij}_{\sigma}\Delta\mathbf{u}_{\tau i} \\ &= \delta\mathbf{u}^T_{sj}\mathbf{K}^{\tau sij}_{T}\Delta\mathbf{u}_{\tau i} \end{aligned} \tag{45}$$

As previously discussed in the derivation of internal and external force vectors in the CUF framework, the tangent stiffness matrix is derived in terms of FNs whose formal expressions result in the invariance of the theory of structural approximation adopted and kinematic models employed in the beam model considered.

6. Numerical results

The present section outlines the proposed case studies and numerical results of hyperelastic higher-order beam models. These models are compared against reference solutions obtained through the conventional 3 D finite element method implemented in ABAQUS. Utilizing these models enables the prediction of displacement and stress distributions within structures under highly deformed equilibrium states, necessitating higher-order theories for accurate computation of displacement and

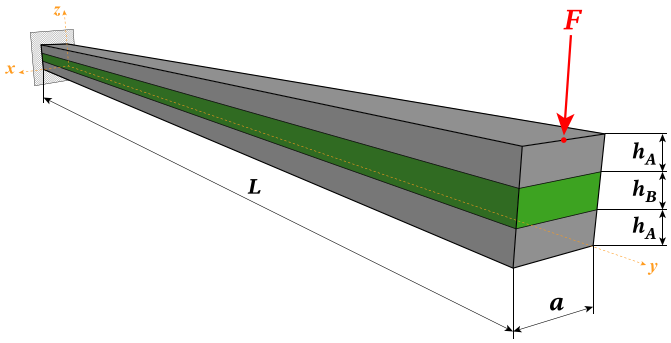

Fig. 3. Cantilever multilayered beam: geometrical features and boundary conditions.

Table 1
Cantilever multilayered beam: material properties.

	c_{10} [MPa]	c_{01} [MPa]	μ [MPa]	ν [-]	E [MPa]	$D_1 = 2/k$ [MPa^{-1}]
Material A	30	−4	52	0.2	124.8	$2.8846 \cdot 10^{-8}$
Material B	10	1.5	23	0.3	59.8	$4.0133 \cdot 10^{-8}$

stress components. Subsequently, various hyperelastic material models will be investigated in the following analyses, focusing on exploring the impact of the mathematical models adopted on the static response of the structure.

6.1. Cantilever multilayered beam under concentrated load

The static analysis of a multilayered compressible beam is performed as the first assessment study case. A cantilever square cross-section beam of total length L and lateral side a is made of three layers of two different hyperelastic materials. The thickness of the layers is $h_A = h_B = a/3$. In the following, the cross-section side a is considered fixed to $a = 1$ cm, and two different geometrical conditions will be analyzed: a thick beam with slender ratio $L/a = 10$ and a slender beam for which instead $L/a = 100$. The beam is clamped at $y = 0$ cm and subjected to a concentrated transversal load at the free end. Geometry and boundary conditions are depicted in Fig. 3.

Each hyperelastic layer is described by adopting the decoupled Mooney–Rivlin model for the isochoric component and the classical quadratic model for the volumetric component of the strain energy function:

$$\Psi = \quad \Psi_{vol}(J) + \bar{\Psi}(\bar{I}_1, \bar{I}_2) = \frac{1}{D_1}(J-1)^2 + c_{10}(\bar{I}_1 - 3) + c_{01}(\bar{I}_2 - 3) \qquad (46)$$

where c_{10} and c_{01} are material constants typically obtained from experimental data fit, and $D_1 = 2/k$ with k the bulk modulus. In the Mooney–Rivlin material model, the initial shear modulus is defined as $\mu = 2(c_{10}+c_{01})$, by which it is possible to determine straightforwardly the Young modulus E and bulk modulus k. The material parameters adopted are listed in Table 1.

A convergence analysis is performed to assess the accuracy and the efficiency of the 1D beam models regarding displacement distribution, considering both the thick and slender beam cases. The effects of the mathematical models adopted on the mechanical response of the structure are investigated, analyzing the influence of the finite element discretization along the beam axis and the cross-section kinematics, assessing initially LW models. In this investigation, parabolic L9 (nine-node) or cubic L16 (sixteen-node) expansion models in the cross-section discretization are initially adopted. The models adopted are depicted in Fig. 4. The results of higher-order 1D CUF elements are comprehensively compared with the numerical reference results obtained by the 3 D ABAQUS model, both in terms of displacements and stress distribution. In the case of the thick beam, 8190 C3D20R hexahedral elements (20-node quadratic brick 3 D elements, reduced integration) are adopted in the discretization of the beam. Instead, 31320 C3D20R elements are employed in discretizing the slender beam due to hexahedral models' aspect ratio constraints. Instead, the same 1D CUF mathematical models for thick and slender beams will be adopted, considering N B4 finite elements along the beam axis and N_E L9 or L16 parabolic or cubic expansion elements. In the following investigations, the numerical results will be expressed in terms of non-dimensional quantities, here defined:

$$\bar{u}_z = \frac{u_z}{L} \qquad \%_{diff}(\cdot) = \frac{(\cdot)_{\text{1D CUF}} - (\cdot)_{\text{3D}}}{(\cdot)_{\text{3D}}} \cdot 100\ \% \qquad \lambda = \frac{F}{F_{max}} \qquad (47)$$

where u_z is the transversal displacement component and F_{max} is the maximum final load considered in the static analysis, when specified. The accuracy is measured in terms of the percentage difference between the proposed 1D CUF results and the 3 D ABAQUS solution. At the same time, the computational costs are expressed in terms of the total degrees of freedom (DOFs) of the discretization adopted. In the following analysis, the numerical solver is coupled with a load-control procedure, considering $F_{max} = 50$ N for the thick beam, and $F_{max} = 1$ N for the slender beam.

Table 2 presents the non-dimensional transversal displacement $\bar{u}_z$ measured at the point-load application for the thick beam case. The investigation is presented for various load conditions, ranging from small to moderate/large displacement regimes, assessing both model efficiency and accuracy. Similarly, Table 3 presents the results obtained for the static analysis of the slender beam. In both scenarios, accurate predictions were consistently observed across convergence studies. Fig. 5 shows the equilibrium path of the thick beam considering the most accurate beam axis discretization model and various cross-section expansion models, comparing the computed path with the full 3 D ABAQUS solution. The same comparison is proposed in Fig. 6 for the slender beam. In the case of the slender beam, a perfect matching of the numerical solutions obtained from different cross-section models is observed. Instead, in the case of the thick beam, minor differences are obtained at the large displacement regime for highly nonlinear equilibrium states.

For slender beams, percentage differences below 1 % are observed across all mathematical models, indicating negligible influence of the cross-section expansion or kinematic model selection along the beam axis on the displacement distribution. However, increasing the number of finite elements along the beam axis in thick beams generally improves accuracy across all load conditions. Specifically, the most accurate results are obtained with higher-order models and enriched cross-section

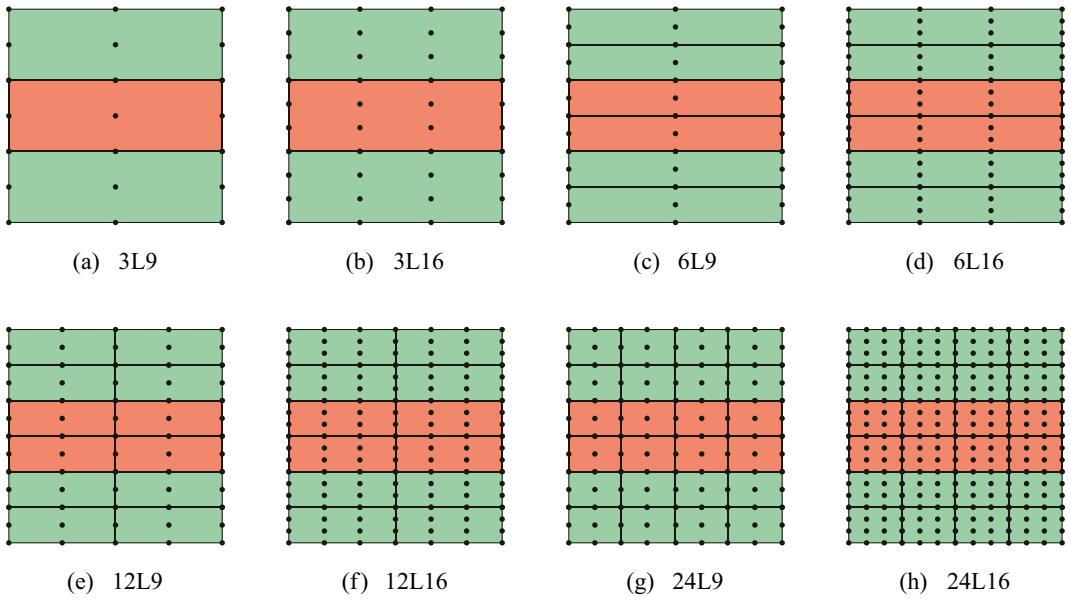

Fig. 4. Cantilever multilayered beam: cross-section expansion adopted, LE models.

kinematics. Convergence is achieved with 20 B4 cubic elements along the beam axis. Although minor differences were noted across cases, consistent results were obtained for each discretization, mainly when refined cross-section kinematics were employed.

In the case of the slender beam, accurate results are already achieved with a less refined model, regarding, as an example, 10 B4 cubic elements along the beam axis, for a total save in terms of DOFs of around 95 % with respect to the computational cost required by the convergent 3 D model. In the following, a stress analysis is performed to assess the accuracy and convergence of the models in terms of stress distributions.

Furthermore, the influence of the theory of structure approximation is investigated in terms of the expansion model adopted. A comparison for the slender and thick beam cases is proposed comparing the results obtained by adopting LE models with those obtained with TE models. In the case of TE models, the most accurate mathematical model along the beam axis is adopted. Thus, 20 B4 cubic elements are adopted along the beam axis discretization. Table 4 shows the computed non-dimensional transversal displacement $\bar{u}_z$ for the slender beam case, measured again at the point-load application, computed adopting various TE models, comparing the results with the already obtained values from LE models and 3 D ABAQUS solution. The same comparison is proposed in Table 5 for the thick beam case. Finally, Fig. 7 shows the whole equilibrium paths computed adopting higher-order TE models for slender and thick beams. Accurate solutions are obtained when lower-order models are considered for the slender beam. Instead, higher-order models are required for the thick beam. In general, the linear TE1 model cannot predict the equilibrium path at moderate displacement regimes due to the limitation of classical beam theories.

Fig. 8 shows the through-the-thickness distribution of the Cauchy's stress components for the thick beam with slender ratio $L/a = 10$, measured at $x = a/2$ (symmetry section) and $y/L = 0.25$, comparing the proposed results with the fully 3 D ABAQUS solution taken as reference. The same comparison is proposed in the slender beam case, with a slender ratio $L/a = 100$, in Fig. 10. The stress distributions presented here are obtained by adopting the most accurate finite element discretization along the beam axis observed in the previous convergence analysis; thus, 20 B4 are again employed. The cross-section expansions listed before are again adopted to investigate the influence of the theory of structure approximation on the computation of the three-dimensional stress components.

Regarding the normal stress components, accurate results regarding σ_{yy} and σ_{zz} are obtained. A perfect matching with respect to the adopted 3 D reference is observed. Minor differences are evident in the σ_{xx} component. Observing the proposed distribution of transverse shear stress σ_{yz}, non-zero values at the beam edges and non-symmetric distributions of the considered stress component are observed. Fig. 9 shows the comparison between the Cauchy's stress component in the actual reference frame and the correspondent first Piola–Kirchhoff stress component, respectively σ_{yz} and P_{yz} in different load conditions. This comparison shows that the equilibrium conditions and stress compatibility are guaranteed for the first Piola–Kirchhoff stress tensor, for which the equilibrium equation is valid due to the Total Lagrangian finite element formulation adopted. In the case of Cauchy's stress tensor, the compatibility conditions are not guaranteed since conservative loads are considered. Thus, non-zero components of shear stresses must arise in highly deformed states to balance the externally conservative or non-conservative applied load [23].

Since Cauchy's stress components are directly related to the deformation gradient, which is now measuring (in the material reference frame) the moderate/large strain regime, the non-symmetric distribution of actual stresses arises from the classical distribution of transverse shear stresses due to the equilibrium condition given by Eq. (8). The same comparison is proposed for the slender beam in Fig. 11, and similar considerations can be addressed.

6.2. *Analysis of* 0°/90° *reinforced laminate under transverse and axial pressure loads*

The next case study proposed is the static analysis of a multilayered fiber-reinforced laminated beam. Two different geometrical and load conditions are considered to analyze the influence of higher-order models on the mechanical response of the beam. In the first condition, a cantilever square cross-section beam of total length $L_b = 100$ mm and lateral side $a = 5$ mm made of two equal layers with different fiber orientations is considered under a uniform transversal pressure applied at the top surface; furthermore, a uniaxial tension test is performed, analyzing a beam with length $L_s = 20$ mm and the lateral side $a = 5$ mm. The thickness of the two layers is considered equal thus $h_L = a/2$. Thanks to the symmetry of the two structures and the load conditions applied, only one half of the structure has been analyzed in the following numerical

Table 2
Cantilever Mooney–Rivlin multilayered beam: convergence analysis for the case $L/h = 10$. Non-dimensional transversal displacement $\bar{u}_z$ measured at the point-load application. Comparison between 1D CUF beam models and ABAQUS 3 D reference solutions for different load conditions. In brackets, the percentage difference between the actual results and the 3 D model results is proposed.

		u_z/L				
B4	Expansion	F = 10 N	F = 20 N	F = 30 N	F = 40 N	DOFs
10	3 L9	0.31503(2.75 %)	0.53003(2.34 %)	0.65552(2.55 %)	0.73188(3.27 %)	1953
	3 L16	0.31488(2.79 %)	0.52975(2.39 %)	0.65514(2.61 %)	0.73140(3.33 %)	3720
	6 L9	0.31511(2.72 %)	0.53021(2.31 %)	0.65577(2.52 %)	0.73217(3.23 %)	3627
	6 L16	0.31489(2.79 %)	0.52977(2.39 %)	0.65517(2.61 %)	0.73143(3.33 %)	7068
	12 L9	0.31665(2.25 %)	0.53335(1.73 %)	0.66011(1.87 %)	0.73758(2.52 %)	6045
	12 L16	0.31731(2.04 %)	0.53484(1.46 %)	0.66242(1.53 %)	0.74070(2.10 %)	12,369
	24 L9	0.31720(2.08 %)	0.53457(1.51 %)	0.66203(1.58 %)	0.74022(2.17 %)	10,881
	24 L16	0.31784(1.88 %)	0.53610(1.22 %)	0.66464(1.20 %)	0.74402(1.67 %)	22,971
15	3 L9	0.31528(2.67 %)	0.53042(2.27 %)	0.65594(2.49 %)	0.73230(3.21 %)	2898
	3 L16	0.31514(2.71 %)	0.53016(2.32 %)	0.65561(2.54 %)	0.73189(3.27 %)	5520
	6 L9	0.31543(2.63 %)	0.53074(2.21 %)	0.65637(2.43 %)	0.73281(3.15 %)	5382
	6 L16	0.31516(2.71 %)	0.53023(2.31 %)	0.65569(2.53 %)	0.73200(3.26 %)	10,488
	12 L9	0.31750(1.99 %)	0.53481(1.46 %)	0.66183(1.61 %)	0.73948(2.27 %)	8970
	12 L16	0.31860(1.65 %)	0.53723(1.02 %)	0.66548(1.07 %)	0.74438(1.62 %)	18,354
	24 L9	0.31836(1.72 %)	0.53666(1.12 %)	0.66467(1.19 %)	0.74336(1.75 %)	16,146
	24 L16	0.31946(1.38 %)	0.53944(0.61 %)	0.66937(0.49 %)	0.75020(0.85 %)	34,086
20	3 L9	0.31541(2.63 %)	0.53060(2.24 %)	0.65612(2.46 %)	0.73247(3.19 %)	3843
	3 L16	0.31528(2.67 %)	0.53038(2.28 %)	0.65584(2.51 %)	0.73212(3.24 %)	7320
	6 L9	0.31561(2.57 %)	0.53103(2.16 %)	0.65668(2.38 %)	0.73312(3.11 %)	7137
	6 L16	0.31533(2.66 %)	0.53050(2.26 %)	0.65600(2.48 %)	0.73232(3.21 %)	13,908
	12 L9	0.31807(1.81 %)	0.53571(1.30 %)	0.66279(1.47 %)	0.74050(2.13 %)	11,895
	12 L16	0.31963(1.33 %)	0.53901(0.69 %)	0.66764(0.75 %)	0.74704(1.27 %)	24,339
	24 L9	0.31920(1.46 %)	0.53806(0.86 %)	0.66630(0.95 %)	0.74533(1.49 %)	21,411
	24 L16	0.32088(0.94 %)	0.54224(0.09 %)	0.67323(0.08 %)	0.75558(0.14 %)	45,201
ABQ	8190 C3D20R	0.32393	0.54275	0.67269	0.75663	115,314

Table 3
Cantilever Mooney–Rivlin multilayered beam: convergence analysis for the case $L/h = 100$. Non-dimensional transversal displacement $\bar{u}_z$ measured at the point-load application. Comparison between 1D CUF beam models and ABAQUS 3 D reference solutions for different load conditions. In brackets, the percentage difference between the actual results and the 3 D model results is proposed.

		u_z/L				
B4	Expansion	F = 0.2 N	F = 0.4 N	F = 0.6 N	F = 0.8 N	DOFs
10	3 L9	0.49028(0.15 %)	0.66983(0.12 %)	0.74601(0.11 %)	0.78720(0.11 %)	1953
	3 L16	0.48472(1.28 %)	0.66559(0.75 %)	0.74285(0.54 %)	0.78466(0.43 %)	3720
	6 L9	0.49028(0.15 %)	0.66983(0.12 %)	0.74601(0.11 %)	0.78720(0.11 %)	3627
	6 L16	0.49028(0.15 %)	0.66983(0.12 %)	0.74601(0.11 %)	0.78720(0.11 %)	7068
	12 L9	0.49028(0.15 %)	0.66984(0.12 %)	0.74602(0.11 %)	0.78720(0.11 %)	6045
	12 L16	0.49029(0.15 %)	0.66984(0.12 %)	0.74602(0.11 %)	0.78720(0.11 %)	12,369
	24 L9	0.49029(0.15 %)	0.66984(0.12 %)	0.74602(0.11 %)	0.78720(0.11 %)	10,881
	24 L16	0.49029(0.15 %)	0.66984(0.12 %)	0.74602(0.11 %)	0.78720(0.11 %)	22,971
15	3 L9	0.49055(0.10 %)	0.67015(0.07 %)	0.74637(0.06 %)	0.78760(0.06 %)	2898
	3 L16	0.48499(1.23 %)	0.66592(0.71 %)	0.74321(0.49 %)	0.78507(0.38 %)	5520
	6 L9	0.49056(0.10 %)	0.67016(0.07 %)	0.74637(0.06 %)	0.78760(0.06 %)	5382
	6 L16	0.49056(0.09 %)	0.67016(0.07 %)	0.74637(0.06 %)	0.78760(0.06 %)	10,488
	12 L9	0.49056(0.09 %)	0.67016(0.07 %)	0.74638(0.06 %)	0.78760(0.06 %)	8970
	12 L16	0.49056(0.09 %)	0.67016(0.07 %)	0.74638(0.06 %)	0.78761(0.06 %)	18,354
	24 L9	0.49056(0.09 %)	0.67016(0.07 %)	0.74638(0.06 %)	0.78761(0.06 %)	16,146
	24 L16	0.49056(0.09 %)	0.67016(0.07 %)	0.74638(0.06 %)	0.78761(0.06 %)	34,086
20	3 L9	0.49068(0.07 %)	0.67029(0.05 %)	0.74651(0.05 %)	0.78774(0.04 %)	3843
	3 L16	0.49068(0.07 %)	0.67029(0.05 %)	0.74651(0.05 %)	0.78774(0.04 %)	7320
	6 L9	0.49068(0.07 %)	0.67029(0.05 %)	0.74651(0.05 %)	0.78774(0.04 %)	7137
	6 L16	0.49068(0.07 %)	0.67029(0.05 %)	0.74651(0.05 %)	0.78774(0.04 %)	13,908
	12 L9	0.49069(0.07 %)	0.67029(0.05 %)	0.74651(0.05 %)	0.78774(0.04 %)	11,895
	12 L16	0.49069(0.07 %)	0.67030(0.05 %)	0.74651(0.05 %)	0.78775(0.04 %)	24,339
	24 L9	0.49069(0.07 %)	0.67030(0.05 %)	0.74651(0.05 %)	0.78774(0.04 %)	21,411
	24 L16	0.49069(0.07 %)	0.67030(0.05 %)	0.74652(0.05 %)	0.78775(0.04 %)	45,201
ABQ	31320 C3D20R	0.49102	0.67065	0.74685	0.78806	445,758

investigations. Geometry and boundary conditions for the two proposed problems are depicted in Fig. 12(a) and Fig. 12(b), respectively.

Each layer is modeled by adopting the fiber-reinforced hyperelastic strain energy function analyzed in [30,46], where the classical Neo-Hookean isotropic component is coupled with the quadratic model for the fiber-reinforcement effects given by I_4, and a stabilized volumetric strain energy function:

$$\Psi = \Psi_{vol}(J) + \Psi_{iso}(I_1, I_2) + \Psi_{aniso}(I_4) = \frac{\mu}{2}(I_1 - 3) + \frac{\lambda}{2}(J-1)^2 - \mu \log J + \gamma(I_4 - 1)^2 \tag{48}$$

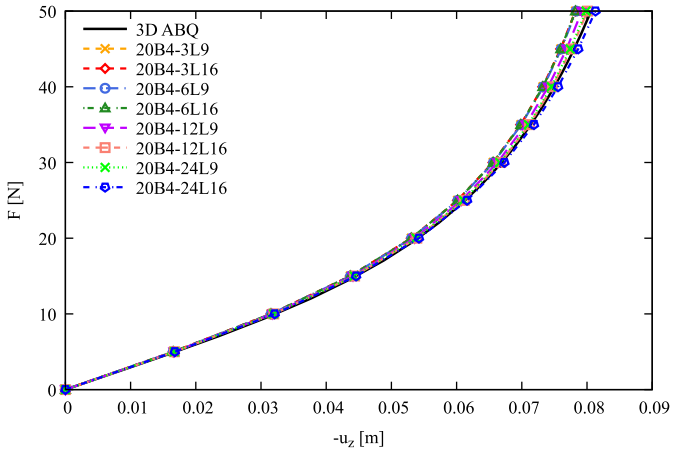

Fig. 5. Cantilever Mooney–Rivlin multilayered beam, case $L/h = 10$: equilibrium paths for the thick beam computed with the most accurate finite element discretization along the beam axis. Transversal displacement u_z measured at the point-load application.

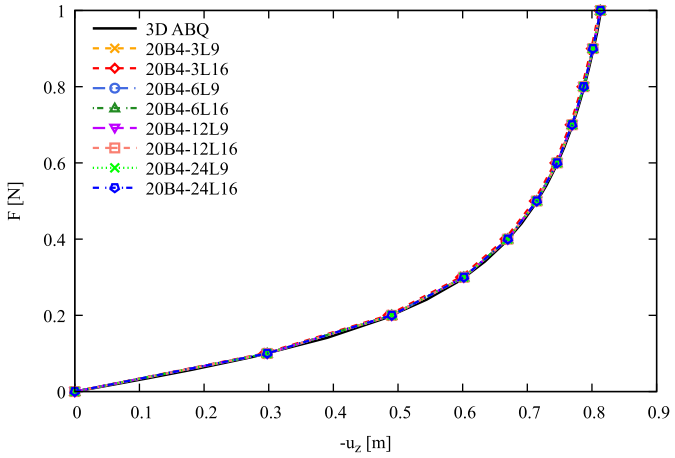

Fig. 6. Cantilever Mooney–Rivlin multilayered beam, case $L/h = 100$: equilibrium paths for the slender beam computed with the most accurate finite element discretization along the beam axis. Transversal displacement u_z measured at the point-load application.

Table 4
Cantilever Mooney–Rivlin multilayered beam, case $L/h = 100$: comparison between LW models and ESL models results, for different load conditions. Non-dimensional transversal displacement $\bar{u}_z$ measured at the point-load application. In brackets, the percentage difference between the actual results and the 3 D model results is proposed.

B4	Expansion	F = 0.2 N	F = 0.4 N	F = 0.6 N	F = 0.8 N	DOFs
10	24 L16	0.49029$^{(0.15\ \%)}$	0.66984$^{(0.12\ \%)}$	0.74602$^{(0.11\ \%)}$	0.78720$^{(0.11\ \%)}$	22,971
15	24 L16	0.49056$^{(0.09\ \%)}$	0.67016$^{(0.07\ \%)}$	0.74638$^{(0.06\ \%)}$	0.78761$^{(0.06\ \%)}$	34,086
20	24 L16	0.49069$^{(0.07\ \%)}$	0.67030$^{(0.05\ \%)}$	0.74652$^{(0.05\ \%)}$	0.78775$^{(0.04\ \%)}$	45,201
20	TE1	0.45957$^{(6.41\ \%)}$	0.64623$^{(3.64\ \%)}$	0.72864$^{(2.44\ \%)}$	0.77361$^{(1.83\ \%)}$	549
	TE2	0.49051$^{(0.10\ \%)}$	0.67014$^{(0.08\ \%)}$	0.74638$^{(0.06\ \%)}$	0.78762$^{(0.06\ \%)}$	1098
	TE3	0.49053$^{(0.10\ \%)}$	0.67017$^{(0.07\ \%)}$	0.74641$^{(0.06\ \%)}$	0.78766$^{(0.05\ \%)}$	1830
	TE4	0.49055$^{(0.10\ \%)}$	0.67018$^{(0.07\ \%)}$	0.74642$^{(0.06\ \%)}$	0.78767$^{(0.05\ \%)}$	2745
ABQ	31,320 C3D20R	0.49102	0.67065	0.74685	0.78806	445,758

where $\mu = 1$ MPa is the infinitesimal shear modulus, $\lambda = 4$ MPa is the Lame constant, and $\gamma = 0.375$ MPa. The two layers are considered in a global stacking sequence, with the top-layer fibers oriented along the beam axis direction and the bottom-layer fibers in the transversal direction, oriented along the x axis. The effects of the mathematical models adopted on the mechanical response of the structure are investigated, analyzing in particular the influence of the cross-section kinematic. From the previously discussed analysis, 20 B4 cubic finite elements along the beam axis are adopted for convergence reasons. Instead, different cross-section expansions will be considered, again adopting parabolic L9 (nine-node) or cubic L16 (sixteen-node) expansions. The computational costs are expressed again in terms of the total DOFs of the discretization adopted. The two configurations presented are now analyzed separately.

6.2.1. *Uniform transverse pressure case*

Table 6 reports the numerical solution of the transversal displacement u_z, measured at the point "A" of the beam represented in Fig. 12(a),

Table 5
Cantilever Mooney–Rivlin multilayered beam, case $L/h = 10$: comparison between LE models results and TE models results, for different load conditions. Non-dimensional transversal displacement $\bar{u}_z$ measured at the point-load application. In brackets, the percentage difference between the actual results and the 3 D model results is proposed.

B4	Expansion	F = 10 N	F = 20 N	F = 30 N	F = 40 N	DOFs
10	24 L16	0.31784(1.88 %)	0.53610(1.22 %)	0.66464(1.20 %)	0.74402(1.67 %)	22,971
15	24 L16	0.31946(1.38 %)	0.53944(0.61 %)	0.66937(0.49 %)	0.75020(0.85 %)	34,086
20	24 L16	0.32088(0.94 %)	0.54224(0.09 %)	0.67323(0.08 %)	0.75558(0.14 %)	45,201
20	TE1	0.28572(11.80 %)	0.49389(9.00 %)	0.62281(7.41 %)	0.70373(6.99 %)	549
	TE2	0.31289(3.41 %)	0.52639(3.01 %)	0.65099(3.23 %)	0.72672(3.95 %)	1098
	TE3	0.31387(3.11 %)	0.52791(2.73 %)	0.65270(2.97 %)	0.72848(3.72 %)	1830
	TE4	0.31376(3.14 %)	0.52758(2.80 %)	0.65215(3.05 %)	0.72776(3.82 %)	2745
ABQ	8190 C3D20R	0.32393	0.54275	0.67269	0.75663	115,314

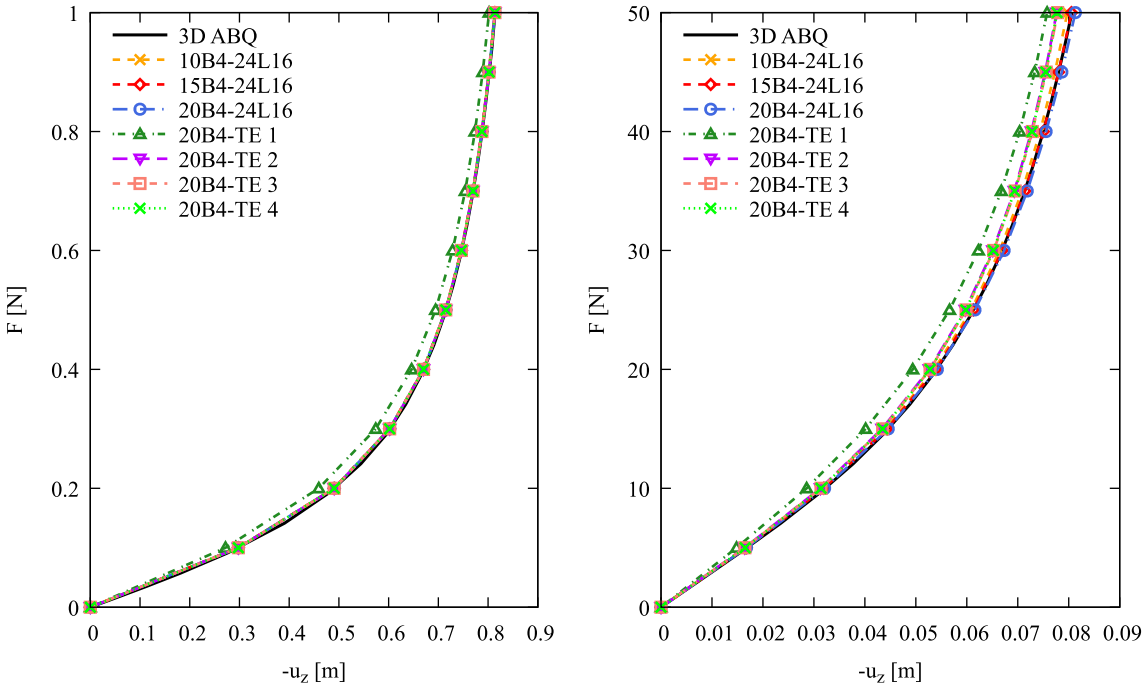

(a) Slender beam, $L/h = 100$ **(b)** Thick beam, $L/h = 10$

Fig. 7. Cantilever Mooney–Rivlin multilayered beam: equilibrium paths for the slender and thick beam, comparison between LE expansion models and TE expansion models.

in correspondence of the symmetry section. The results are proposed for different values of the applied transversal pressure, comparing the solution obtained via different cross-section expansion models. Fig. 13 shows the equilibrium path obtained adopting the previously listed discretization models along the beam cross-section, obtained via the static analysis of the structure adopting an arc-length type constraint in the numerical solver. From the small to moderate/large displacement regime, the numerical solutions perfectly match between different cross-section kinematic models investigated. Fig. 14 illustrates the through-the-thickness distribution of the transversal displacement u_z measured at the $x-$symmetry section foy $y = 40$ mm, near y-symmetry section. An almost linear behavior of the through-the-thickness transversal displacement component is observed.

In terms of displacement distributions and equilibrium paths, each model adopted predicts consistent solutions. Convergence is already achieved when pure LW discretization models, such as 2L9 and 2L16 expansions, are considered. Convergence is now discussed in terms of stress distributions.

Fig. 15 shows the through-the-thickness distribution of the Cauchy's stress components and first Piola–Kirchhoff stress tensor when a uniform pressure applied of $p = 162$ kPa is considered. Stress components are measured at the symmetry section, for $x = 0$ and $y = 40$ mm, near the y-symmetry section. The three-dimensional stress components are consistently computed for each cross-section kinematic model adopted; perfectly matching results are observed in the case of normal σ_{yy} component. Consistent results are also obtained in the case of remaining normal components. Minor differences are attributed to the adoption of refined kinematics along the cross-section in the z-direction. In particular, looking at the transverse normal component and σ_{yz} shown in Fig. 15(d), major differences, such as discontinuities and non-zero values at the beam edges are observed. Theoretically consistent results are obtained when higher-order models are considered. This behavior is explained by the strong influence in hyperelastic soft structures of large strains that are directly influencing the distribution of the first Piola–Kirchhoff stress tensor when computed from the second Piola–Kirchhoff stress tensor $\mathbf{S}$ and considering conservative loads in the proposed Total-Lagrangian displacement-based finite element formulation, as proposed in the comparison of P_{yz} stress component in Fig. 16.

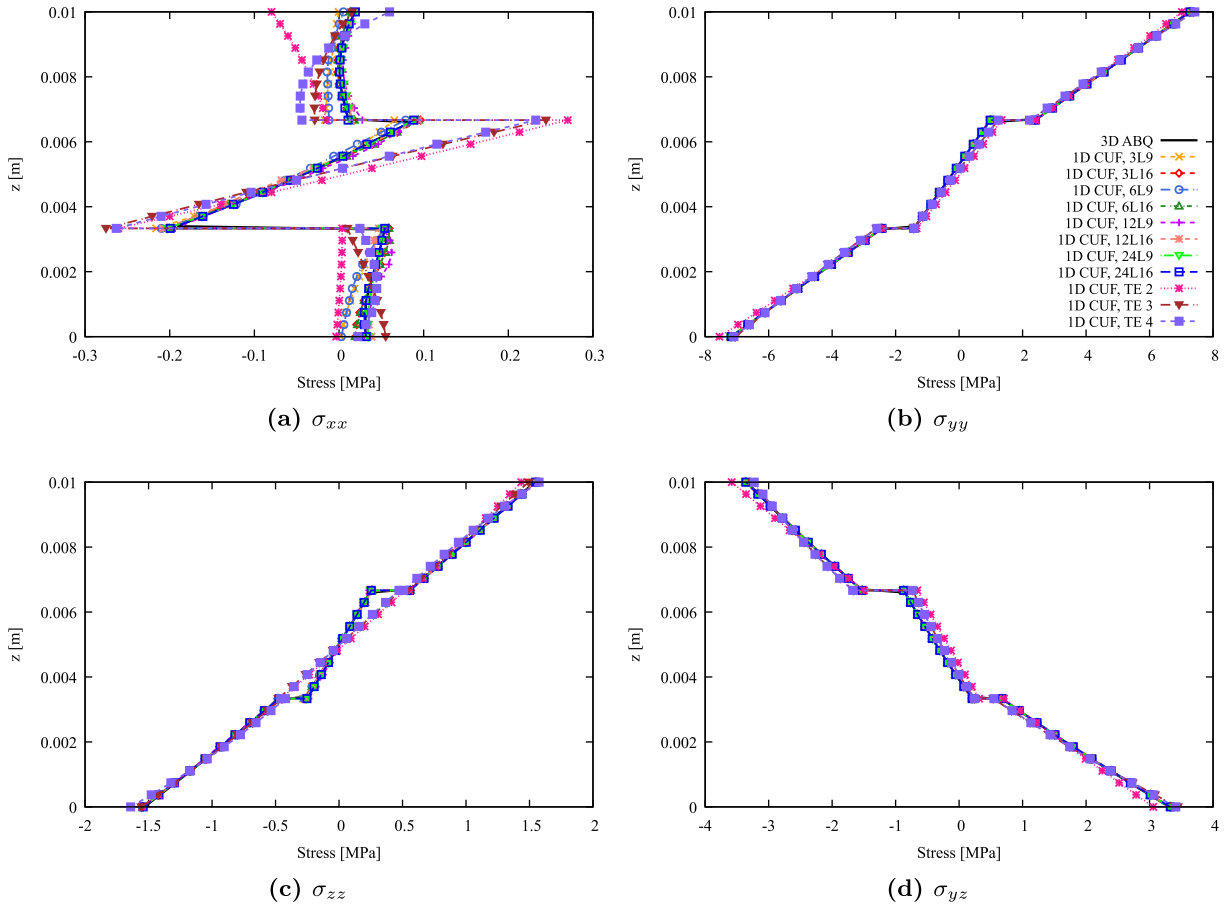

Fig. 8. Cantilever Mooney–Rivlin multilayered beam, case $L/h = 10$: through-the-thickness stress distribution along for $y/L = 0.25$ and $x = a/2$. Comparison between 1D CUF solution and ABAQUS 3 D reference.

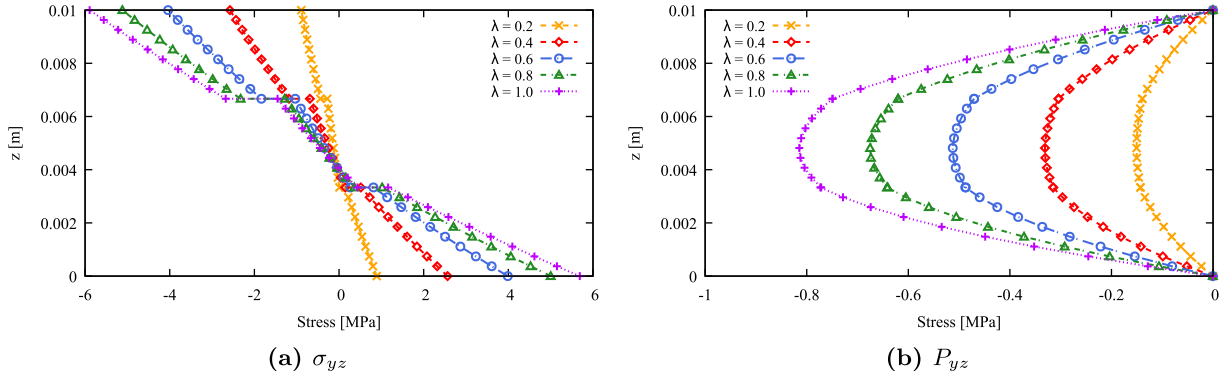

Fig. 9. Cantilever Mooney–Rivlin multilayered beam, case $L/h = 10$: through-the-thickness distribution of the transverse stress components σ_{yz} and P_{yz} for $y/L = 0.25$ and $x = a/2$, for different load conditions.

6.2.2. *Uniaxial tension case*

The numerical solution presented in Table 7 showcases the horizontal displacement u_y measured at point "A" of the beam represented in Fig. 12(b), specifically at the end section for $y = 10$ mm. In these investigations, the previously addressed cross-section kinematics are adopted in the discretization models. These results are provided across various applied transversal pressure values, comparing solutions derived from different cross-section expansion models. Furthermore, Fig. 17(a) illustrates the equilibrium path for the uniaxial tension test obtained through the static analysis, employing a numerical solver based on the load-control procedure, so considering a $p_{max} = 30$ MPa as end load and 20 equal load steps. The numerical solutions exhibit perfect alignment from small to moderate/large strains. Moreover, Fig. 17(b) shows the cross-sectional displacement measured again at the symmetry section, investigating the influence of the applied traction pressure on the cross-section warping, stretching, and other local effects.

Fig. 18 shows the through-the-thickness distribution of the vertical displacement u_z, measured at the symmetry section $y = 0$ mm and $x = 0$ mm, computed for various cross-section kinematics when $p = 13.5$ MPa is considered. A slight parabolic behavior of the transversal displacement component is observed.

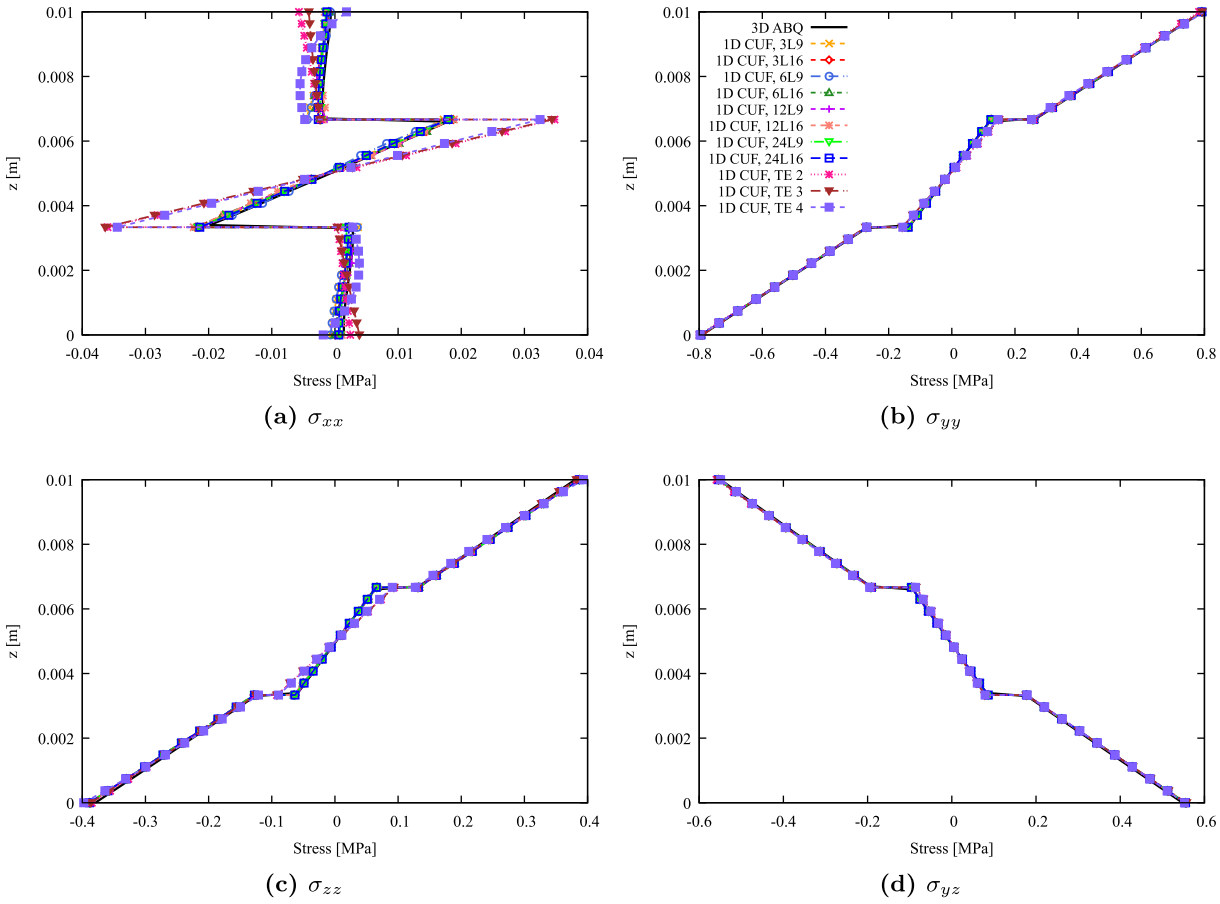

Fig. 10. Cantilever Mooney–Rivlin multilayered beam, case $L/h = 100$: through-the-thickness stress distribution along for $y/L = 0.25$ and $x = a/2$. Comparison between 1D CUF solution and ABAQUS 3 D reference.

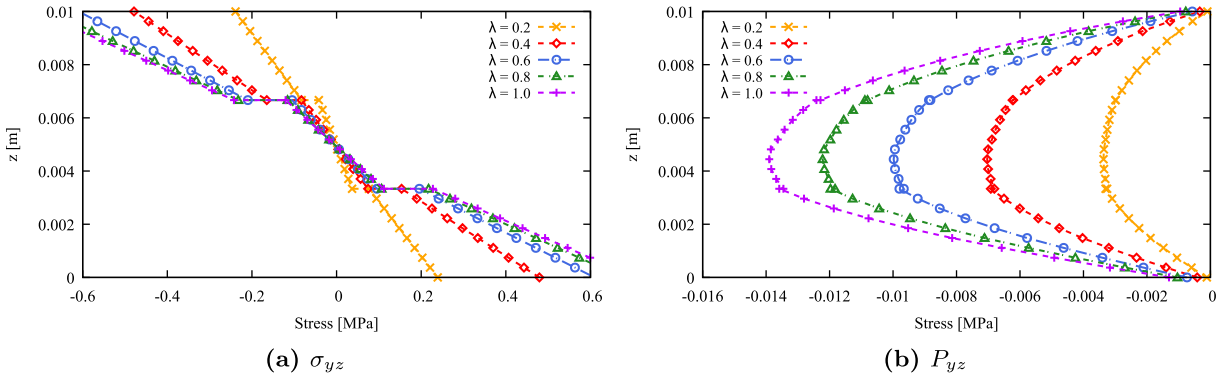

Fig. 11. Cantilever Mooney–Rivlin multilayered beam, case $L/h = 100$: through-the-thickness distribution of the transverse stress components σ_{yz} and P_{yz} for $y/L = 0.25$ and $x = a/2$, for different load conditions.

Again, in terms of displacement distributions and equilibrium paths, each model adopted allows consistent predictions. Convergence is already achieved when pure LW discretization models, such as 2L9 and 2L16 expansions, are considered. Convergence is again discussed in terms of stress distributions. Fig. 19 shows the through-the-thickness distribution of Cauchy's stress components when a uniform traction pressure of $p = 15.5$ MPa is considered. Stress components are measured at the symmetry section, for $x = 0$ and $y = 2.5$ mm, near the y-symmetry section. The three-dimensional stress components are consistently computed for each cross-section kinematic model adopted; perfectly matching results are observed in the case of normal σ_{yy}, instead consistent results are also obtained in the case of σ_{xx}, which do not adopt refined discretization in the x-direction. Significant differences such as discontinuities and different global and local slopes are observed in the case of normal σ_{zz} component. In this case, due to the effects of the large strains, refined structural theories and kinematics models are required to compute accurately the deformation gradient $\mathbf{F}$ thus the second Piola–Kirchhoff stress tensor $\mathbf{S}$. Therefore, coarser cross-section discretization can lead to inconsistent results. This is also observed for the transverse normal component σ_{yz} shown in Fig. 19(d), where discontinuities and non-zero values at the beam edges are observed or coarser discretization, inconsistently with the equilibrium and compatibility

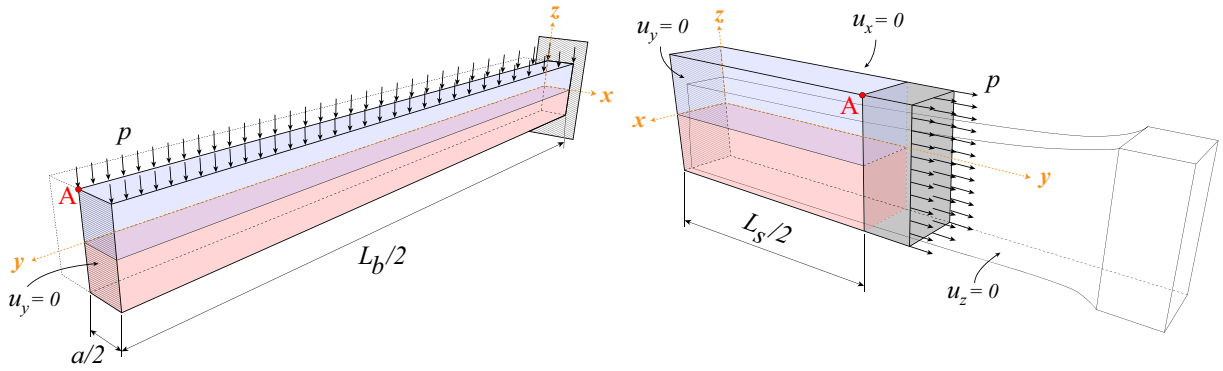

(a) Bending problem (b) Uniaxial test problem

Fig. 12. Hyperelastic 0°/90° laminate: geometrical features and boundary conditions.

Table 6
Hyperelastic 0°/90° laminate, uniform transverse pressure case: convergence analysis, transversal displacement component $-u_z$. Comparison between various cross-section LE models adopted, for different load conditions.

	$-u_z$ [mm]				
Model	p = 2.52 kPa	p = 17.33 kPa	p = 81.94 kPa	p = 309.93 kPa	DOFs
2L9	6.7890	15.2934	28.1352	48.2150	2745
2L16	6.7976	15.2973	28.1128	48.1427	5124
4L9	6.7954	15.3064	28.1584	48.2707	4941
4L16	6.7976	15.3109	28.1658	48.2870	9516
8L9	6.7966	15.3088	28.1620	48.2807	9333
8L16	6.7978	15.3113	28.1663	48.2875	18,300
10L9	6.7967	15.3090	28.1623	48.2810	11,529
10L16	6.7978	15.3113	28.1663	48.2877	22,692
20L9	6.7977	15.3109	28.1656	48.2869	19,215
20L16	6.7981	15.3119	28.1671	48.2892	39,711

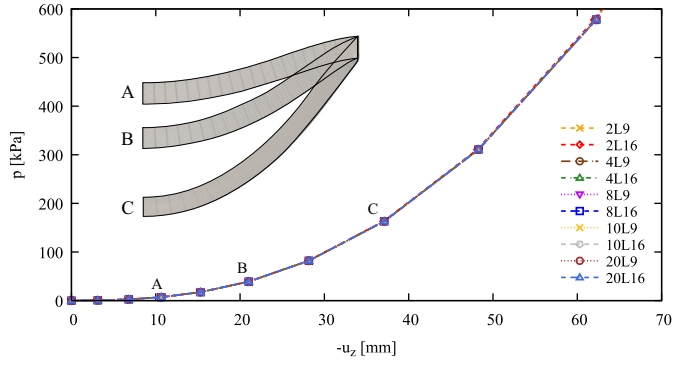

Fig. 13. Hyperelastic 0°/90° laminate, uniform transverse pressure case: equilibrium path, transversal displacement $-u_z$ versus applies load p. Comparison between paths obtained adopting different cross-section kinematics.

conditions. In the case of refined cross-section models, instead, the global equilibrium conditions are satisfied, and non-symmetric global stress distributions are observed due to local shear effects. At the contrary, the compatibility and equilibrium conditions are perfectly guaranteed in the case of P_{yz} component, shown in Fig. 20, for which a non-symmetric distribution is observed.

6.3. Analysis of 0°/45°/−45°/0° reinforced laminate under transverse and axial pressure loads

The last case study presented is the static analysis of a four-layer laminated beam. In the following investigations, the effect of the structural theory adopted on the mechanical behavior of the structure is investigated again. Two different configurations are now addressed to analyze the impact of the large displacement-rotation or large strain regime. In the first configuration, a cantilever square cross-section beam of total length L_b = 100 mm and lateral side a = 10 mm is considered under a uniform transversal pressure applied at the top surface as shown in Fig. 21(a); likewise, a different configuration with L_s = 50 mm and lateral side a = 10 mm is analyzed under a uniform uniaxial traction pressure, as shown in Fig. 21(b). The beam now comprises four layers of equal thickness $h_l = a/4$, with different fiber orientations. Thanks to the symmetry of the two structures and the load conditions applied, only one-fourth of the structure has been considered in the following numerical investigations.

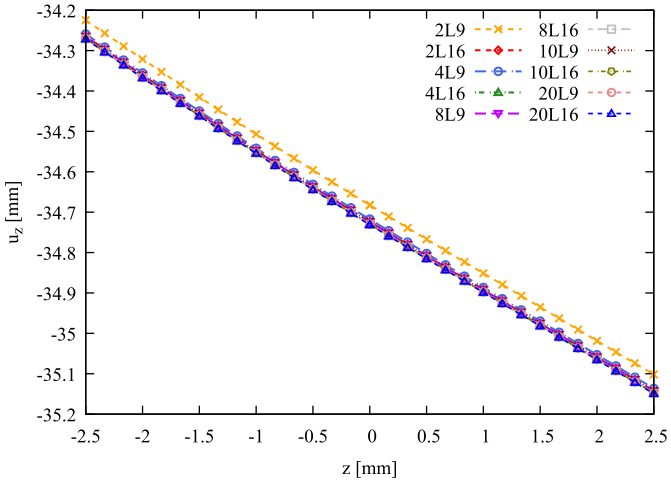

Fig. 14. Hyperelastic 0°/90° laminate, uniform transverse pressure case: through-the-thickness transversal displacement u_z distribution, measured at $y = 40$ mm, for an applied transversal pressure of $p = 162$ kPa. Comparison between various cross-section expansion models.

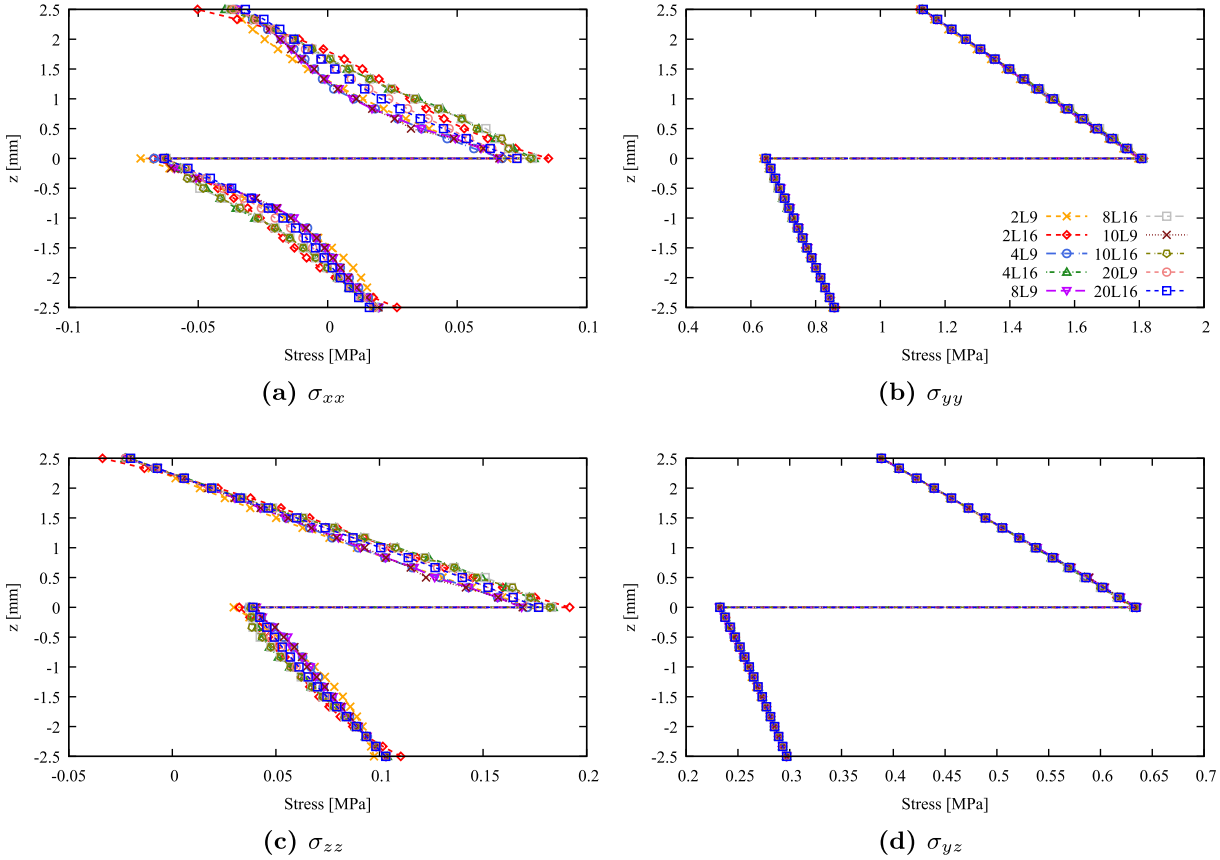

(a) σ_{xx} (b) σ_{yy}

(c) σ_{zz} (d) σ_{yz}

Fig. 15. Hyperelastic 0°/90° laminate, uniform transverse pressure case: through-the-thickness stress components distribution, measured at $y = 40$ mm and $x = 0$ mm at the x-symmetry section, for an applied transverse pressure of $p = 162$ kPa.

The material is modeled by adopting again the strain energy function detailed in Section 6.2; thus, Eq. (48) is again considered. The material constants are again $\mu = 1$ MPa, $\lambda = 4$ MPa, and $\gamma = 0.375$ MPa, as previously investigated. Four different layers of fibrous soft materials are considered, where the fiber orientation can vary in the $x - y$ plane. The continuous fiber reinforcement, as detailed in the anisotropic hyperelastic constitutive law modeling, is represented here by the unitary versor $\mathbf{a}_0 = (\sin\theta, \cos\theta, 0)$, where θ is measured with respect to y axis in the $x - y$ plane. The global stacking sequence (from the bottom to the top layer) is $0°/45°/-45°/0°$. As previously addressed, convergence considerations lead to utilizing 20 B4 cubic finite elements along the beam axis. Additionally, various cross-section expansions, such as parabolic L9 (nine-node) or cubic L16 (sixteen-node), are explored. Computational cost is once more quantified as the total degrees of freedom of the discretization employed.

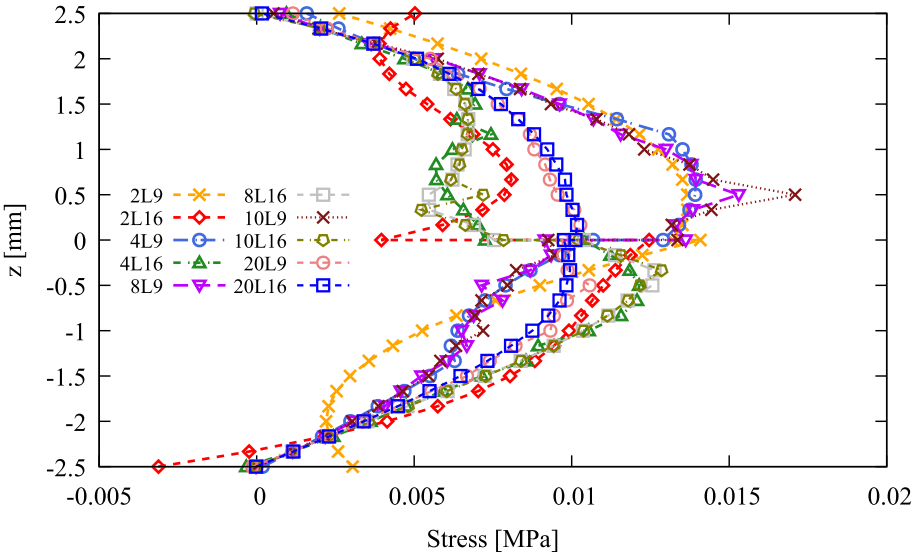

Fig. 16. Hyperelastic 0°/90° laminate, uniform transverse pressure case: through-the-thickness distribution of P_{yz} component, measured at $y = 40$ mm and $x = 0$ mm at the x-symmetry section, for an applied transverse pressure of $p = 162$ kPa.

Table 7
Hyperelastic 0°/90° laminate, uniaxial tension test: convergence analysis, horizontal displacement component u_y measured at the point A. Comparison between various cross-section LE models adopted for different load conditions.

	u_y [mm]				
Model	$p = 4.5$ MPa	$p = 12$ MPa	$p = 18$ MPa	$p = 24$ MPa	DOFs
2L9	7.7553	14.6649	18.3484	21.2875	2745
2L16	7.7574	14.6690	18.3536	21.2935	5124
4L9	7.7563	14.6670	18.3507	21.2898	4941
4L16	7.7574	14.6686	18.3525	21.2916	9516
8L9	7.7571	14.6689	18.3533	21.2930	9333
8L16	7.7579	14.6699	18.3545	21.2930	18,300
10L9	7.7571	14.6690	18.3534	21.2931	11,529
10L16	7.7579	14.6699	18.3545	21.2943	22,692
20L9	7.7578	14.6700	18.3548	21.2946	19,215
20L16	7.7580	14.6703	18.3534	21.2943	39,711

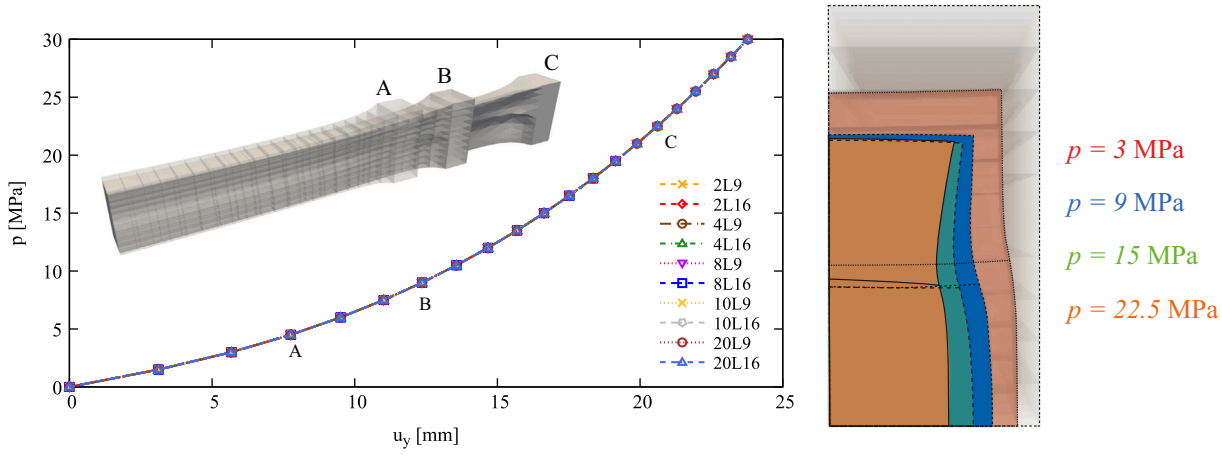

(a) Equilibrium path (b) Cross-section kinematics for 10L16

Fig. 17. Hyperelastic 0°/90° laminate, uniaxial tension test: equilibrium path, transversal displacement u_y versus applies load p. Comparison between paths obtained adopting different cross-section kinematics.

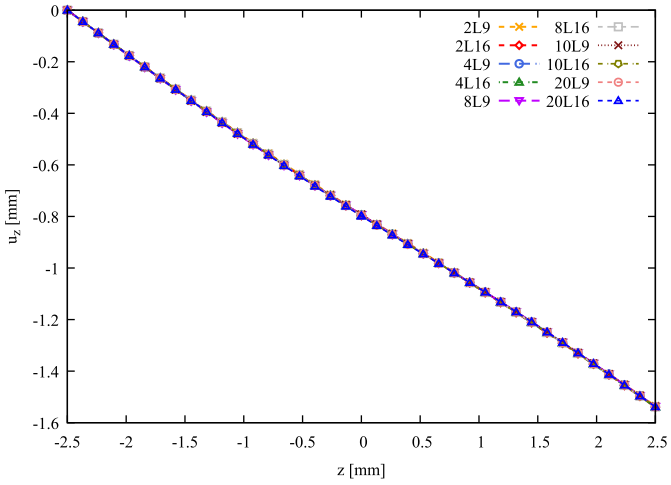

Fig. 18. Hyperelastic 0°/90° laminate, uniaxial tension test: through-the-thickness transversal displacement u_z distribution, measured at the symmetry section for $x = 0$ mm, obtained with different cross-section kinematics.

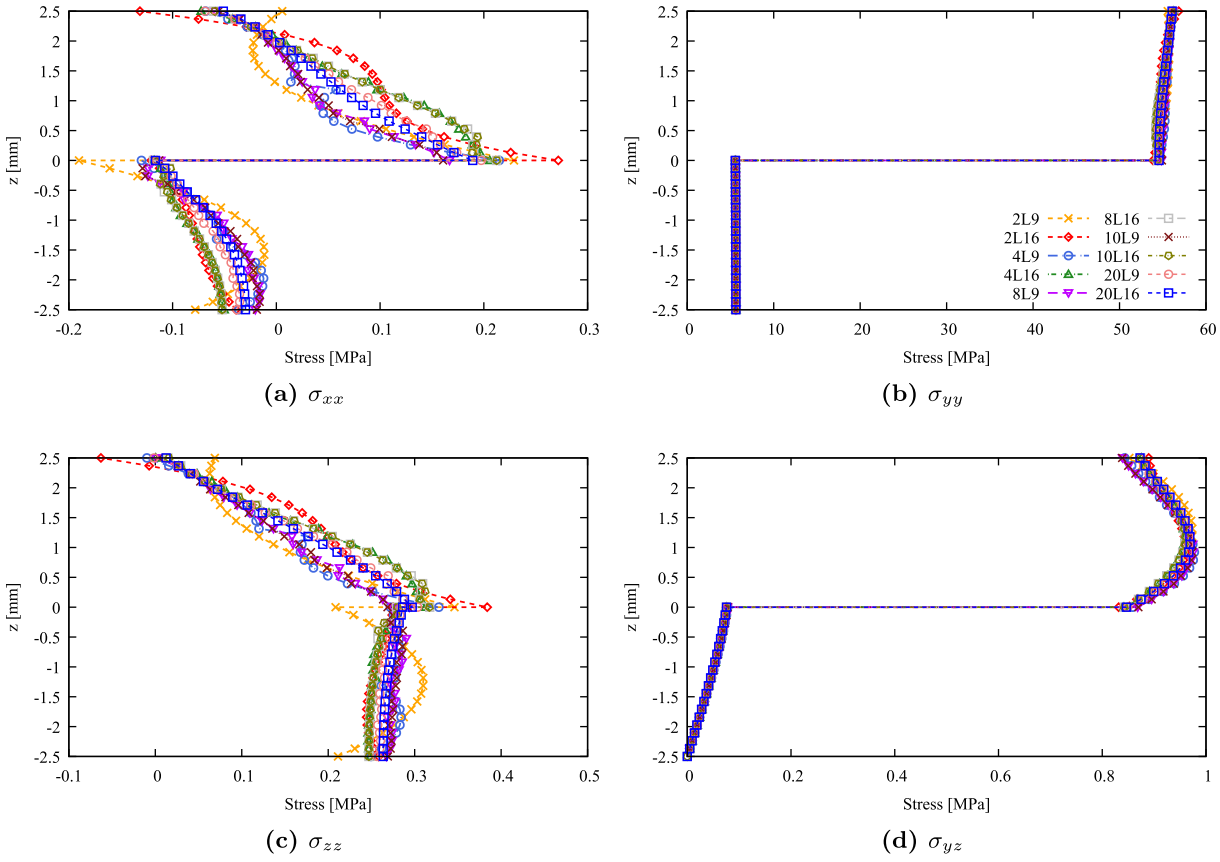

Fig. 19. Hyperelastic 0°/90° laminate, uniaxial tension test: through-the-thickness stress components distribution, measured at $y = 2.5$ mm and $x = 0$ mm, for an applied traction pressure of $p = 13.5$ MPa. Comparison between stress components obtained from different cross-section expansion models.

6.3.1. Uniform transversal pressure case

Table 8 reports the numerical solution of the transverse displacement u_z, measured at the point "A" of the beam represented in Fig. 21(a), in correspondence of the symmetry section. The results are proposed for different values of the applied transversal pressure, comparing the solution obtained via different cross-section expansion models. Fig. 22 depicts the equilibrium path obtained adopting the previously listed discretization models along the beam cross-section, obtained via the static analysis of the structure adopting an arc-length type constraint. From the small to moderate/large displacement regime, the numerical solutions perfectly match between models. Fig. 23 illustrates the through-the-thickness transversal displacement distribution measured at the $x-$ symmetry section foy $y = 5$ mm, near y-symmetry section.

Fig. 24 shows the through-the-thickness distribution of normal stress components when a uniform transverse pressure applied of $p = 156.85$ kPa is considered. Stress quantities are measured along the

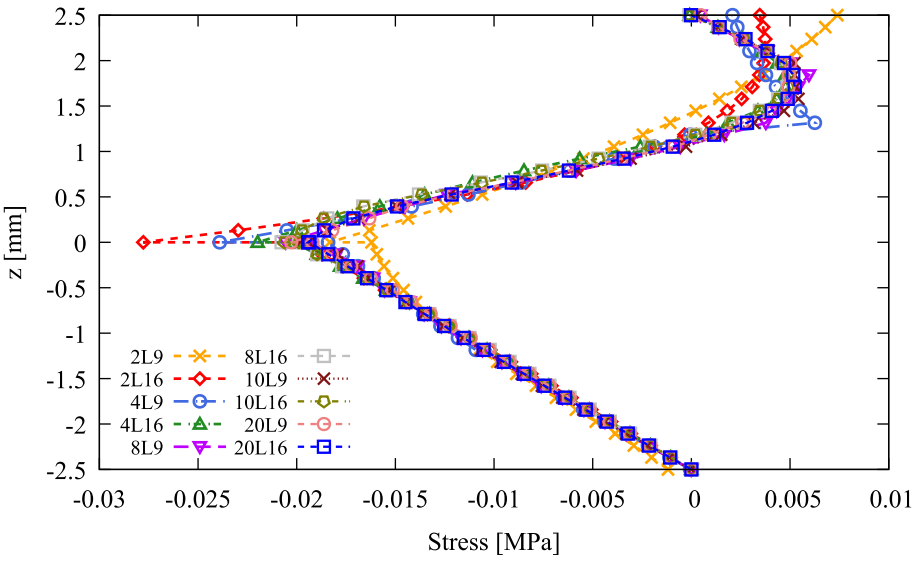

Fig. 20. Hyperelastic 0°/90° laminate, uniaxial tension test: through-the-thickness distribution of P_{yz} component, measured at $y = 2.5$ mm and $x = 0$ mm, for an applied traction pressure of $p = 13.5$ MPa.

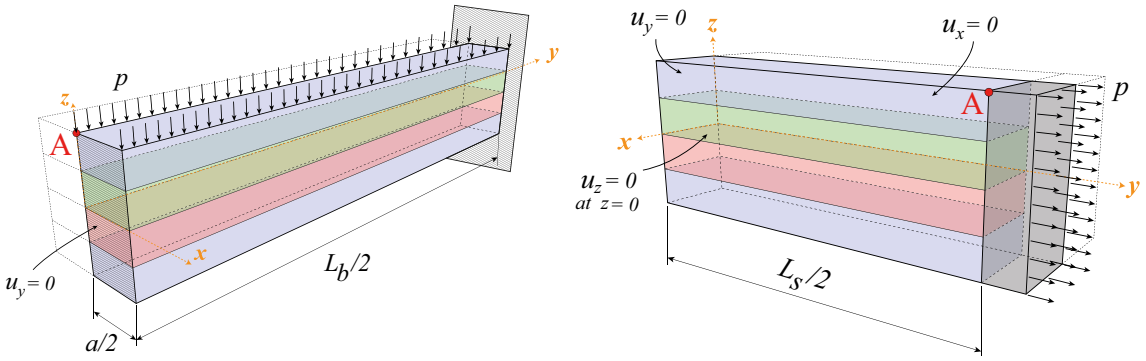

(a) Bending problem (b) Uniaxial test problem

Fig. 21. Hyperelastic 0°/45°/−45°/0° laminate: geometrical features and boundary conditions.

Table 8
Hyperelastic 0°/45°/−45°/0° laminate, uniform transverse pressure case: convergence analysis, transversal displacement component $-u_z$ measured at the symmetry plane. Comparison between various cross-section LE models adopted for different load conditions.

	$-u_z$ [mm]				
Model	$p = 6.01$ kPa	$p = 35.02$ kPa	$p = 156.84$ kPa	$p = 455.65$ kPa	DOFs
4L9	3.9373	13.2365	26.8623	42.2488	4941
4L16	3.9414	13.2501	26.8891	42.2975	9516
8L9	3.9398	13.2444	26.8772	42.2855	9333
8L16	3.9421	13.2523	26.8935	42.3096	18,300
8L92	3.9414	13.2501	26.8891	42.2975	15,555
8L162	3.9414	13.2501	26.8891	42.2975	32,025
12L9	3.9403	13.2460	26.8801	42.2933	13,725
12L16	3.9422	13.2528	26.8945	42.3107	27,084
16L9	3.9405	13.2467	26.8813	42.2957	18,117
16L16	3.9423	13.2529	26.8948	42.3113	35,868

x-symmetry section for $y = 20$ mm. In particular, the comparison between the actual Cauchy's stress components and the correspondent first Piola-Kirchhoff stress components is proposed. For the same load condition, Fig. 25 shows the through-the-thickness distribution of transverse normal and shear stress components related to the PK1 stress tensor.

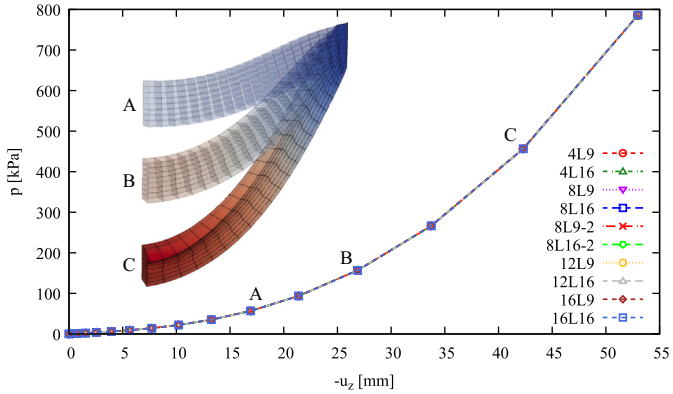

Fig. 22. Hyperelastic $0°/45°/-45°/0°$ laminate, uniform transverse pressure case: equilibrium path, transversal displacement $-u_z$ versus applies load p. Comparison between paths obtained adopting different cross-section kinematics.

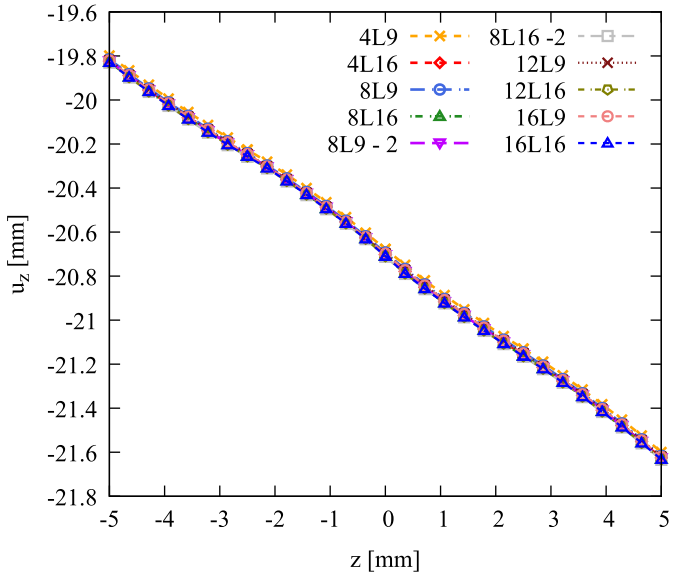

Fig. 23. Hyperelastic $0°/45°/-45°/0°$ laminate, uniform transverse pressure case: through-the-thickness transversal displacement u_z distribution, measured at the symmetry section for $x = 0$ mm, at the section at $y = 20$ mm, obtained with different cross-section kinematics.

Table 9
Hyperelastic $0°/45°/-45°/0°$ laminate, uniaxial tension test: convergence analysis, horizontal displacement component u_y measured at the point A. Comparison between various cross-section LE models adopted for different load conditions.

	u_y [mm]				
Model	$p = 4$ MPa	$p = 8$ MPa	$p = 12$ MPa	$p = 16$ MPa	DOFs
4L9	17.2623	27.6715	35.3166	41.4984	4941
4L16	17.2956	27.7278	35.3888	41.5829	9516
8L9	17.2678	27.6852	35.3383	41.5272	9333
8L16	17.3004	27.7387	35.4052	41.6044	18,300
8L92	17.2949	27.7275	35.3890	41.5837	15,555
8L162	17.3045	27.7461	35.4152	41.6164	32,025
12L9	17.2689	27.6884	35.3437	41.5350	13,725
12L16	17.3008	27.7397	35.4069	41.6066	27,084
16L9	17.2692	27.6892	35.3452	41.5371	18,117
16L16	17.3009	27.7399	35.4073	41.6072	35,868

Stress components reported here show good agreement between different cross-section kinematic models adopted. In particular, consistent predictions are obtained for refined discretization. However, significant differences are evidenced when coarser discretizations are adopted. The proposed normal components σ_{yy} and σ_{zz} shows a perfect superposition of obtained stress distributions. As discussed before, the transverse normal component P_{yz} shown in Fig. 25(d) is satisfying the compatibility and equilibrium conditions, differently for the actual σ_{yz} component

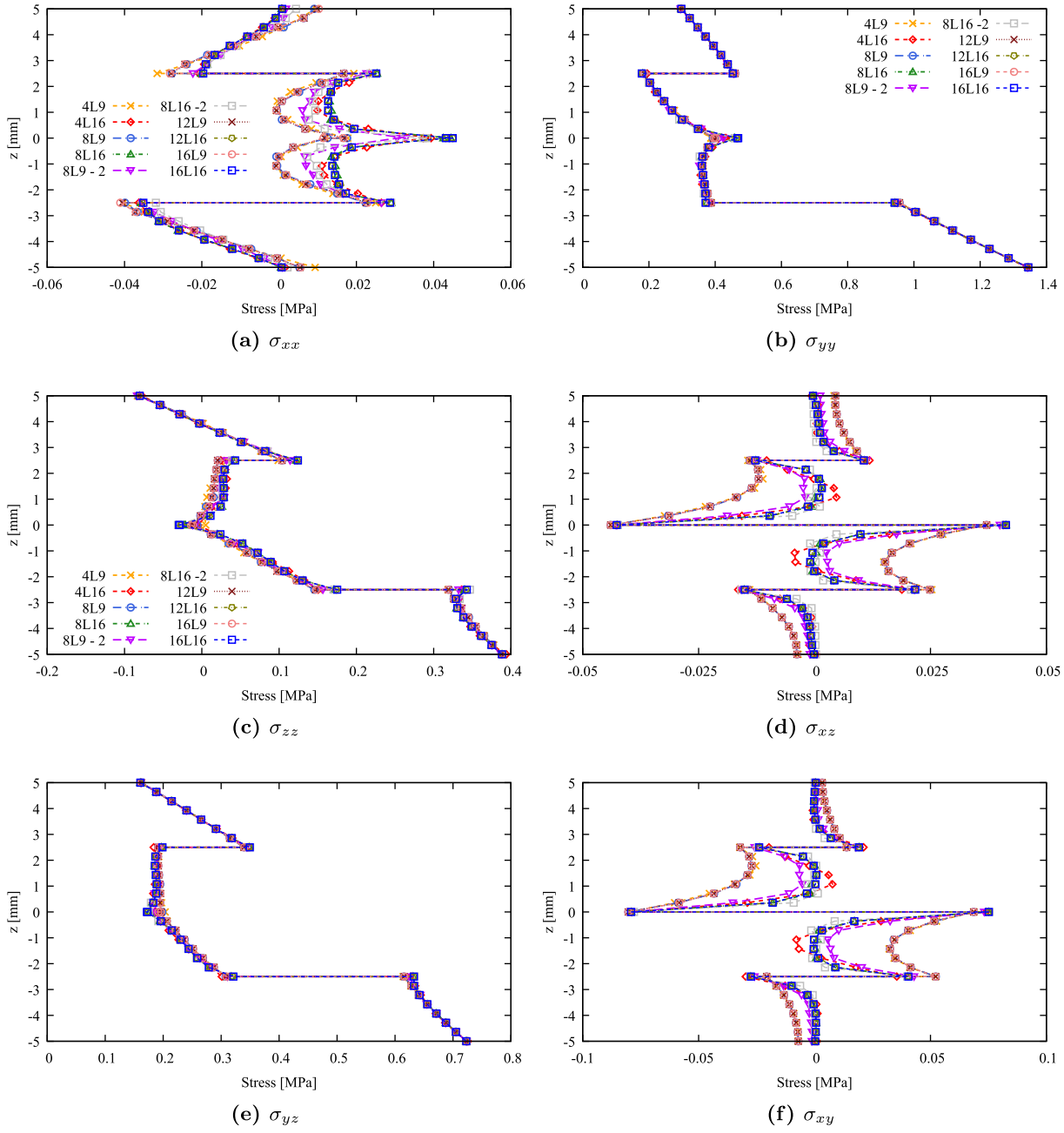

Fig. 24. Hyperelastic 0°/45°/−45°/0° laminate, uniform transversal pressure case: through-the-thickness distribution of normal stress components, measured at $y = 20$ mm and $x = 0$ mm, for an applied transverse pressure of $p = 156.85$ kPa. Comparison between stress components obtained from different cross-section expansion models.

where non-zero values of the transverse shear stresses at the beam edges arise due to the dead load condition considered, under the hypothesis of conservative loads and not follower load. As previously stated, again, large strains directly influence the distribution of the first Piola–Kirchhoff stress tensor when computed from the PK2 stress tensor **S**.

6.3.2. *Uniaxial tension case*

The following discussion presents and comments on the results proposed for the uniaxial tension test. The numerical solution presented in Table 9 showcases the horizontal displacement u_y measured at point "A" of the beam represented in Fig. 21(b), specifically at the end section for $y = 25$ mm. In this investigation, the previously addressed cross-section models are adopted in the mathematical models. These results are provided across various applied traction pressure values. Furthermore, Fig. 26(a) illustrates the equilibrium path for the uniaxial tension test obtained through the static analysis, employing a numerical solver based on the load-control procedure, so considering a $p_{max} = 20$ MPa as end load and 15 equal load steps. The numerical solutions exhibit perfect matching from small to moderate/large strains. Moreover, Fig. 26(b) shows the cross-sectional displacement measured again at the symmetry section, investigating the influence of the applied traction pressure on the cross-section local effects. Fig. 27 shows the through-the-thickness distribution of the vertical displacement u_z, measured at the symmetry section $y = 0$ mm and $x = 0$ mm, computed for various

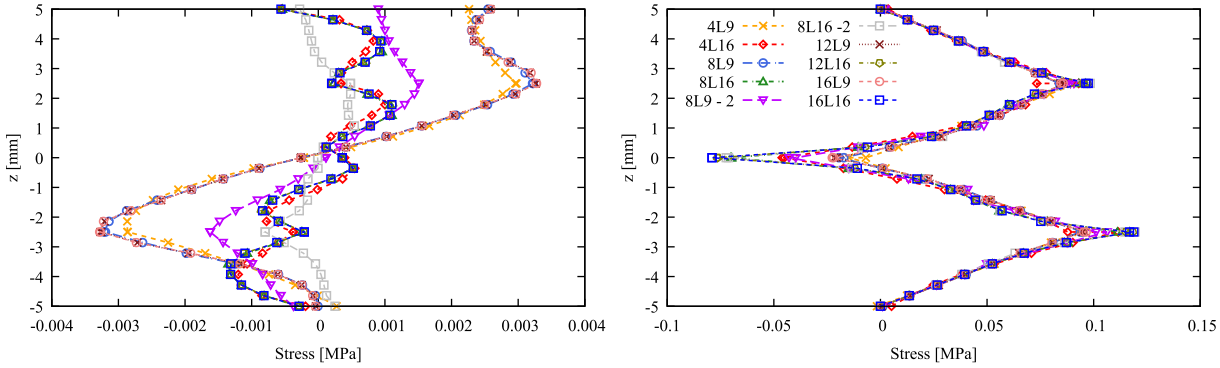

(a) P_{xz} (b) P_{yz}

Fig. 25. Hyperelastic $0°/45°/-45°/0°$ laminate, uniform transversal pressure case: through-the-thickness distribution of transverse normal and shear stress components, measured at $y = 20$ mm and $x = 0$ mm, for an applied transverse pressure of $p = 156.85$ kPa. Comparison between stress components obtained from different cross-section expansion models.

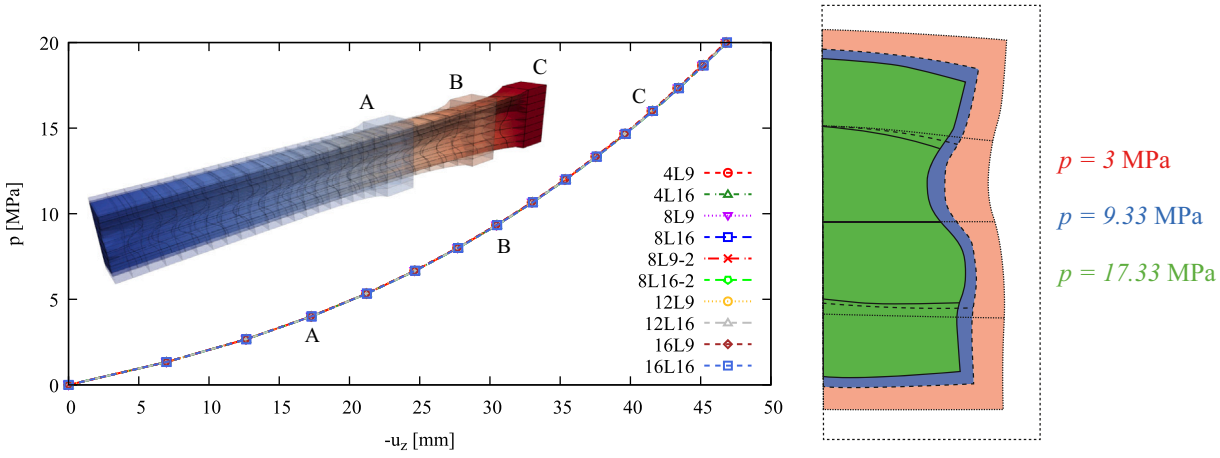

(a) Equilibrium path (b) Cross-section kinematics for 10L16

Fig. 26. Hyperelastic $0°/45°/-45°/0°$ laminate, uniaxial tension test: equilibrium path, transversal displacement u_y versus applies load p. Comparison between paths obtained adopting different cross-section kinematics.

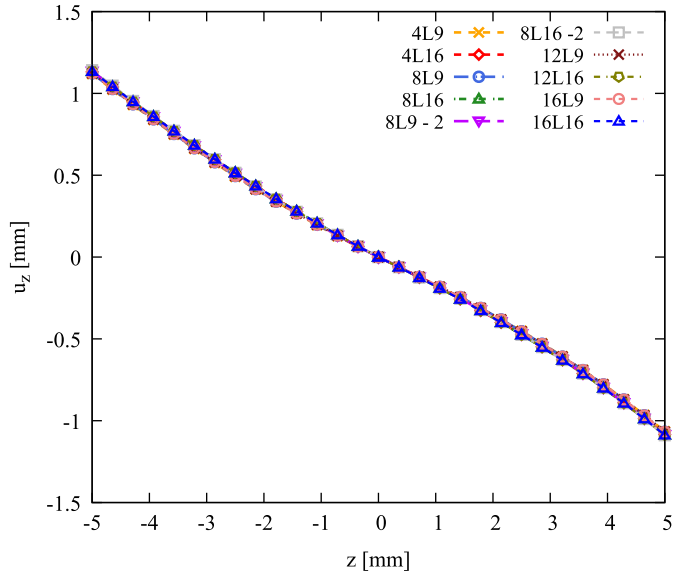

Fig. 27. Hyperelastic $0°/45°/-45°/0°$ laminate, uniaxial tension test: through-the-thickness transversal displacement u_z distribution, measured at the symmetry section for $x = 0$ mm, obtained with different cross-section kinematics.

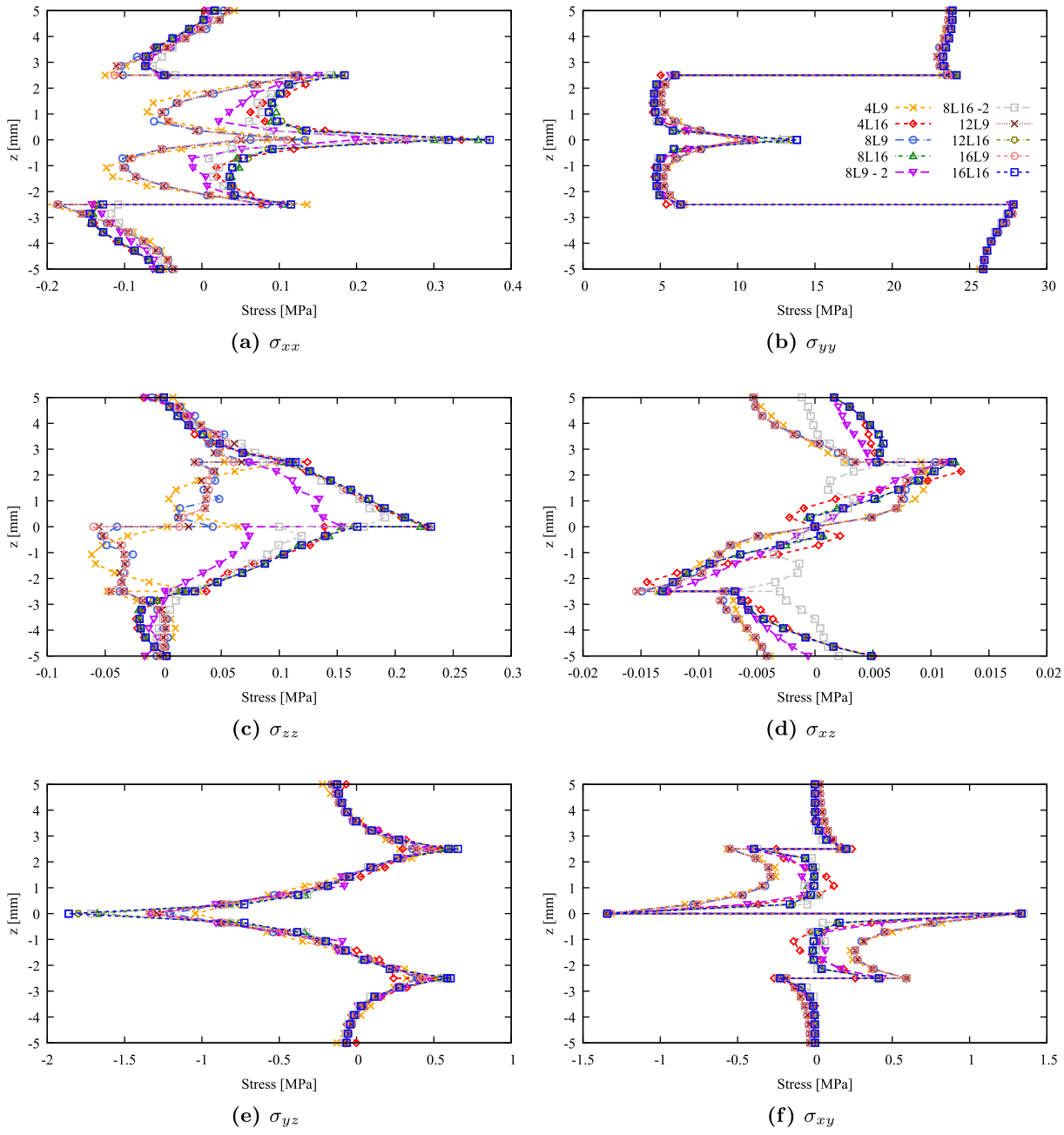

Fig. 28. Hyperelastic $0°/45°/-45°/0°$ laminate, uniaxial tension test: through-the-thickness distribution of normal stress components, measured at $y = 5$ mm and $x = 0$ mm, for an applied traction pressure of $p = 8$ MPa. Comparison between stress components obtained from different cross-section expansion models.

cross-section kinematics when $p = 13.5$ MPa. A parabolic behavior of the through-the-thickness transverse displacement is observed.

Fig. 28 shows the through-the-thickness distribution of normal stress components when a uniform transverse pressure applied of $p = 8$ MPa is considered. Stress quantities are measured along the x-symmetry section for $y = 5$ mm. In particular, the comparison between the actual Cauchy's stress components and the correspondent first Piola–Kirchhoff stress components is proposed. Fig. 29 shows the through-the-thickness distribution of transverse normal and shear stress components when a uniform transverse pressure applied of $p = 8$ MPa is considered. Stress quantities are measured along the x-symmetry section for $y = 5$ mm.

In large strain scenarios, the normal σ_{zz} component present evident disparities, such as discontinuities and variations in global and local gradients when considering different cross-section kinematics. These discrepancies arise due to the influence of significant displacement derivatives, necessitating the adoption of refined structural theories to accurately compute the deformation gradient $\mathbf{F}$, for which the displacement derivatives are approximated using higher-order shape functions are refined polynomial expression of the displacement field. Consequently, employing coarser discretization schemes for cross-sections may yield inconsistent predictions. The transverse normal component P_{yz} shown in Fig. 29(b) is satisfying the compatibility and equilibrium conditions. The necessity of higher-order refined models in large strain hyperelasticity is generally attributed to volumetric locking prevention and computation of physical quantities, such as hydrostatic pressure, without any stabilization technique. A representation of the cross-section warping and deformation along the beam axis is given in Fig. 30. These local effects, such as warping and twisting, are captured

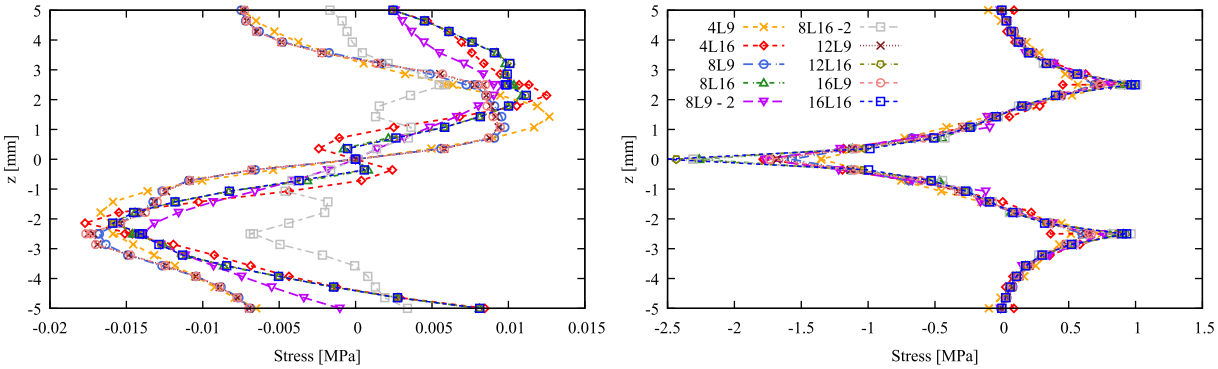

(a) $\mathrm{PK1}_{xz}$ (b) $\mathrm{PK1}_{yz}$

Fig. 29. Hyperelastic $0°/45°/-45°/0°$ laminate, uniaxial tension test: through-the-thickness distribution of transverse normal and shear stress components, measured at $y = 5$ mm and $x = 0$ mm, for an applied traction pressure of $p = 8$ MPa. Comparison between stress components obtained from different cross-section expansion models.

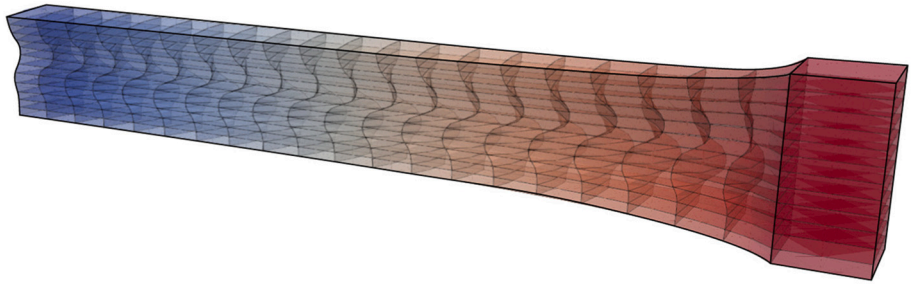

Fig. 30. Hyperelastic $0°/45°/-45°/0°$ laminate, uniaxial tension test: cross-section kinematics representation for an applied traction pressure of $p = 18.6$ MPa, obtained adopting 12L16 cubic element in the cross-section discretization. Displacement magnitude contour.

accurately by refined kinematics. Typically, non-conventional stress distribution within the body arises from these highly deformed states.

7. Conclusions

This paper introduces the unified beam finite element models based on Carrera Unified Formulation (CUF) for the static analysis of multilayered hyperelastic beam structures in the compressible regime. In the classical continuum mechanics framework, hyperelastic constitutive laws expressed in terms of invariants of the deformations have been introduced to describe the mechanical behavior of isotropic and fiber-reinforced soft materials.

The finite element (FE) model introduced in the present work is based on CUF, a framework in which the displacement field is provided as a formal expression independent of the theory of structural approximation adopted. The present study assessed the capabilities of Equivalent-Single-Layer models (ESL) and Layer-Wise (LW) models in a large strain analysis context.

The governing equations have been exploited by the Principle of Virtual Displacement (PVD), rewriting the internal and external force vectors and tangent stiffness matrices in terms of Fundamental Nuclei (FN), invariants of the kinematic assumptions of the FE model adopted. The static nonlinear problem is solved using the Newton–Raphson iterative procedure coupled with an arc-length constraint and load-control procedures. This approach has been validated by comparing the proposed results with reference solutions obtained via full 3 D elasticity solutions, obtained through commercial software.

The results obtained from the present approach demonstrate the accuracy and efficiency of the proposed refined fully nonlinear beam models in the static analysis of multilayered structures, analyzing different geometrical configurations and load conditions. Leveraging the capabilities of unified beam models, the three-dimensional stress state within the structure was accurately analyzed, as well as displacement distributions when large strain problems were considered, underlining the robustness of the proposed methodology. Furthermore, local effects such as warping and twisting were investigated. The proposed CUF-based FE models were also tested regarding equilibrium and compatibility conditions, analyzing in detail the complex three-dimensional stress state arising in highly-nonlinear deformed states then conservative loads are considered.

Future research will extend the present approach to the analysis of biological tissues by adopting higher-order 2 D plate/shell models, analyzing the 3 D displacement and stress field of soft fibrous structures. Furthermore, direction-dependent mechanical properties on structural modal behavior can be explored starting from this implementation of 1D CUF models. Finally, a comprehensive analysis of locking phenomena is intended, including the hybrid formulation (or u/p formulation) in the unified approach of 1D and 2 D CUF-based models.

CRediT authorship contribution statement

Piero Chiaia: Writing – original draft, Visualization, Validation, Software, Methodology. **Alfonso Pagani**: Writing – review & editing, Supervision, Software, Resources, Methodology, Funding acquisition, Conceptualization. **Erasmo Carrera**: Writing – review & editing, Resources, Methodology, Funding acquisition, Conceptualization.

Funding

This project has received funding from the European Research Council (ERC) under the European Union's Horizon 2020 research and innovation programme (Grant agreement No. 850437).

Declaration of competing interest

The authors declare the following financial interests/personal relationships which may be considered as potential competing interests: Alfonso Pagani reports financial support was provided by European Research Council. This project has received funding from the European Research Council (ERC) under the European Union's Horizon 2020 research and innovation programme (Grant agreement No. 850437). If there are other authors, they declare that they have no known competing financial interests or personal relationships that could have appeared to influence the work reported in this paper.

Data availability

Data will be made available on request.

References

[1] Gil AJ. Structural analysis of prestressed saint venant–kirchhoff hyperelastic membranes subjected to moderate strains. Comput Struct 2006 June; 84(15–16):1012–28. https://doi.org/10.1016/j.compstruc.2006.02.009.
[2] Mansouri MR, Beter J, Fuchs PF, Schrittesser B, Pinter G. Quantifying matrix-fiber mechanical interactions in hyperelastic materials. Int J Mech Sci 2021 April; 195(106268):106268. https://doi.org/10.1016/j.ijmecsci.2021.106268.
[3] Guo L, Lv Y, Deng Z, Wang Y, Zan X. Tension testing of silicone rubber at high strain rates. Polym Test 2016 April; 50:270–75. https://doi.org/10.1016/j.polymertesting.2016.01.021.
[4] Chebbi E, Wali M, Dammak F. An anisotropic hyperelastic constitutive model for short glass fiber-reinforced polyamide. Int J Eng Sci 2016 September; 106:262–72. https://doi.org/10.1016/j.ijengsci.2016.07.003.
[5] Huang T, Chen L, Xing X, Yang S. Study on the nonlinear bending behavior of soft slabs subjected to vertical compressions. Extreme Mech Lett 2022 August; 55:101791.101791. https://doi.org/10.1016/j.eml.2022.101791.
[6] Amabili M. Nonlinear damping in large-amplitude vibrations: modelling and experiments. Nonlinear Dyn 2017 October; 93(1):5–18. https://doi.org/10.1007/s11071-017-3889-z.
[7] Henann DL, Chester SA, Bertoldi K. Modeling of dielectric elastomers: design of actuators and energy harvesting devices. J Mech Phys Solids 2013 October; 61(10):2047–66. https://doi.org/10.1016/j.jmps.2013.05.003.
[8] Nitti A, Torre M, Reali A, Kiendl J, De Tullio MD. A multiphysics model for fluid-structure-electrophysiology interaction in rowing propulsion. Appl Math Model 2023 December; 124:414–44. https://doi.org/10.1016/j.apm.2023.08.003.
[9] De Marinis D, Mantegazza A, Coclite A, De Tullio MD. A fluid-structure interaction method for soft particle transport in curved microchannels. Comput Methods Appl Mech Eng 2024 January; 418:116592.116592. https://doi.org/10.1016/j.cma.2023.116592.
[10] Holzapfel GA, Humphrey JD, Ogden RW. Biomechanics of soft biological tissues and organs, mechanobiology, homeostasis and modelling. 2025 January; 22(222): https://doi.org/10.1098/rsif.2024.0361.
[11] Xie F, Qu Y, Li Y, Meng G. Comparative analysis of nonlinear dynamic behaviors of hyperelastic curved structure modelled by different constitutive laws. Eur J Mech A Solids 2024 July; 106:105307. https://doi.org/10.1016/j.euromechsol.2024.105307.
[12] Canales C, Garcia-Herrera C, Rivera E, Macias D, Celentano D. Anisotropic hyperelastic material characterization: stability criterion and inverse calibration with evolutionary strategies. Mathematics 2023 February; 11(4):922.
[13] Crisfield MA, Moita GF, Lyons LPR, Jelenić G. Enhanced lower-order element formulations for large strains. Comput Mech 1995 December; 17(1–2):62–73. https://doi.org/10.1007/BF00356479.
[14] Chamberland É, Fortin A, Fortin M. Comparison of the performance of some finite element discretizations for large deformation elasticity problems. Comput Struct 2010 June; 88(11–12):664–73. https://doi.org/10.1016/j.compstruc.2010.02.007.
[15] Moerman KM, Fereidoonnezhad B, Patrick McGarry J. Novel hyperelastic models for large volumetric deformations. Int J Solids Struct 2020 June; 193-194:474–91.
[16] Van Huyssteen D, Reddy BD. A virtual element method for transversely isotropic hyperelasticity. Comput Methods Appl Mech Eng 2021 December; 386:114108. https://doi.org/10.1016/j.cma.2021.114108.
[17] Li W, Ma H. A nonlinear cross-section deformable thin-walled beam finite element model with high-order interpolation of warping displacement. Thin-Walled Struct 2020 July; 152:106748. https://doi.org/10.1016/j.tws.2020.106748.
[18] Debeurre M, Grolet A, Cochelin B, Thomas O. Finite element computation of nonlinear modes and frequency response of geometrically exact beam structures. J Sound Vib 2023 March; 548:117534. https://doi.org/10.1016/j.jsv.2022.117534.
[19] Cheng J, Zhang R, Ou X, Yao X. A strain gradient quadrature element for geometrically exact beam with torsion warping. Thin-Walled Struct 2024 April; 197:111635. https://doi.org/10.1016/j.tws.2024.111635.
[20] Li W, Ma H, Gao W. Geometrically exact curved beam element using internal force field defined in deformed configuration. Int J Non Linear Mech 2017 March; 89:116–26. https://doi.org/10.1016/j.ijnonlinmec.2016.12.008.
[21] Velayati HR, Kordkheili SAH. A particular manner to observe free-edge effects in hybrid elastomer/composites plates. Compos Part C Open Access 2023 July; 11:100369. https://doi.org/10.1016/j.jcomc.2023.100369.
[22] Rodman U, Zupan D, Šuštar T, Korelc J. Geometrically nonlinear analysis of layered beams using symbolic approach. Compos Struct 2025 January; 351:118583. https://doi.org/10.1016/j.compstruct.2024.118583.
[23] Kulikov GM, Plotnikova SV. On the second piola-kirchhoff and cauchy stress tensors in nonlinear shells subjected to displacement-dependent loads. Mech Adv Mater Struct 2023 February; 31(16):3564–82. https://doi.org/10.1080/15376494.2023.2180121.
[24] Kulikov GM, Plotnikova SV, Mamontov AA. Assessment of second piola–kirchhoff and cauchy stress tensors in finite rotation sandwich and laminated shells under non-conservative pressure loads. Acta Mech 2024 May; 235(7):4489–513. https://doi.org/10.1007/s00707-024-03925-y.
[25] Kulikov GM, Bohlooly M, Plotnikova SV, Kouchakzadeh MA, Mirzavand B. Nonlinear stress analysis of shell structures in buckling and snapping problems by exact geometry solid-shell elements through sampling surfaces formulation. Int J Non Linear Mech 2021 March; 129:103661. https://doi.org/10.1016/j.ijnonlinmec.2020.103661.
[26] Azzara R, Carrera E, Chiaia P, Filippi M, Pagani A, Petrolo M, et al. Geometrically nonlinear static analysis of multi-component structures through variable-kinematics finite elements. Acta Mech 2024 September; 235(12):7003–26. https://doi.org/10.1007/s00707-024-04084-w.
[27] Moruzzi MC, Cinefra M, Bagassi S. Analysis of an acoustic monopole source in a closed cavity via cuf finite elements. Aerotecnica Missili Spazio 2022 August; 101(4):371–85.
[28] Pagani A, Racionero Sánchez-Majano A, Zamani D, Petrolo M, Carrera E. Fundamental frequency layer-wise optimization of tow-steered composites considering gaps and overlaps. Aerotecnica Missili Spazio 2024 April.
[29] Pagani A, Carrera E. Unified one-dimensional finite element for the analysis of hyperelastic soft materials and structures. Mech Adv Mater Struct 2021 December; 30(2):342–55. https://doi.org/10.1080/15376494.2021.2013585.
[30] Chiaia P, Pagani A, Cinefra M, Carrera E. Analysis of transversely isotropic compressible and nearly-incompressible soft material structures by high order unified finite elements. Mech Adv Mater Struct 2023 November; 31(27):1–17. https://doi.org/10.1080/15376494.2023.2273962.
[31] Pagani A, Chiaia P, Carrera E. Vibration of solid and thin-walled slender structures made of soft materials by high-order beam finite elements. Int J Non Linear Mech 2024 April; 160:104634. https://doi.org/10.1016/j.ijnonlinmec.2023.104634.
[32] Ogden RW. Chichester EH Non-linear elastic deformations. New York: Halsted Press; 1984.
[33] Holzapfel GA. Nonlinear solid mechanics. Chichester, West Sussex, UK: John Wiley & Sons; 2000.
[34] Flory PJ. Thermodynamic relations for high elastic materials. Trans Faraday Soc 1961;57:829. https://doi.org/10.1039/TF9615700829.
[35] Carrera E, Cinefra M, Zappino E, Petrolo M. Finite element analysis of structures through unified formulation. Chichester, West Sussex, UK: Wiley; 2014 July.
[36] Carrera E. Historical review of zig-zag theories for multilayered plates and shells. Appl Mech Rev 2003 May; 56(3):287–308. https://doi.org/10.1115/1.1557614.
[37] Carrera E, Demasi L. Classical and advanced multilayered plate elements based upon PVD and RMVT. part 1: derivation of finite element matrices. Int J Numer Methods Eng 2002 June; 55(2):191–231. https://doi.org/10.1002/nme.492.
[38] Carrera E, Pagani A, Augello R. Large deflection of composite beams by finite elements with node-dependent kinematics. Comput Mech 2022 March; 69(6):1481–500. https://doi.org/10.1007/s00466-022-02151-4.
[39] Carrera E, Pagani A, Augello R. On the role of large cross-sectional deformations in the nonlinear analysis of composite thin-walled structures. Arch Appl Mech 2020 November; 91(4):1605–21. https://doi.org/10.1007/s00419-020-01843-8.
[40] Carrera E, Pagani A, Giusa D, Augello R. Nonlinear analysis of thin-walled beams with highly deformable sections. Int J Non Linear Mech 2021 January; 128(103613):103613. https://doi.org/10.1016/j.ijnonlinmec.2020.103613.
[41] Pagani A, Carrera E. Unified formulation of geometrically nonlinear refined beam theories. Mech Adv Mater Struct 2016 September; 25(1):15–31. https://doi.org/10.1080/15376494.2016.1232458.
[42] Reddy JN. Introduction to nonlinear finite element analysis with applications to heat transfer, fluid mechanics, and solid mechanics. New York: Oxford University Press; 2014.
[43] Carrera E. A study on arc-length-type methods and their operation failures illustrated by a simple model. Comput Struct 1994 January; 50(2):217–29. https://doi.org/10.1016/0045-7949(94)90297-6.
[44] Crisfield MA. An arc-length method including line searches and accelerations. Int J Numer Methods Eng 1983 September; 19(9):1269–89. https://doi.org/10.1002/nme.1620190902.
[45] Wu B, Pagani A, Chen WQ, Carrera E. Geometrically nonlinear refined shell theories by carrera unified formulation. Mech Adv Mater Struct 2019 December; 28(16):1–21. https://doi.org/10.1080/15376494.2019.1702237.
[46] Beheshti A, Ansari R. Finite element analysis of compressible transversely isotropic hyperelastic shells. Acta Mech 2023 March; 234(7):3061–79. https://doi.org/10.1007/s00707-023-03536-z.